



AALBORG UNIVERSITY  
DENMARK

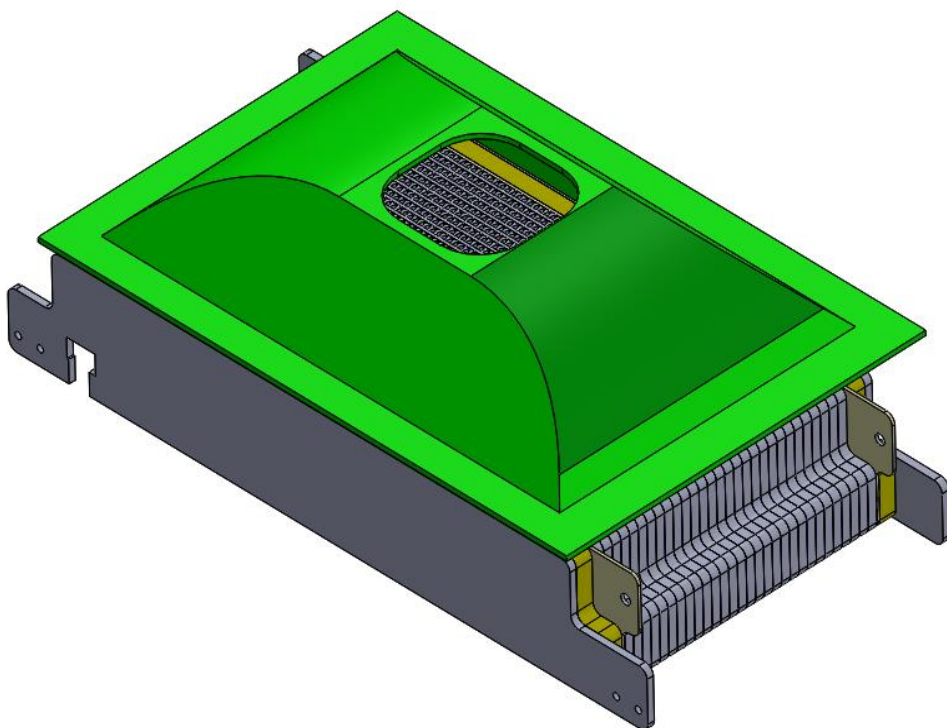
# Numerical Investigation of Manifold Flow Distribution for a Proton-Exchange Membrane Fuel Cell

*Using Computational Fluid Dynamics*

Master Thesis

Stig Eitel Seiferheld

4<sup>th</sup> semester, Thermal Energy and Process Engineering, M.Sc.  
Department of Energy Technology  
Aalborg University







**AALBORG UNIVERSITY**  
STUDENT REPORT

**School of engineering  
and science**

Energy Engineering  
Pontoppidanstræde 111  
9000 Aalborg  
<http://www.ses.aau.dk/>

**Title:**

Numerical Investigation of Manifold Flow Distribution for a Proton-Exchange Membrane Fuel Cell  
*Using Computational Fluid Dynamics*

**Project:**

Master Thesis

**Project period:**

February 2018 - June 2018

**Project group:**

TEPE4-1006

**Group members:**

Stig Eitel Seiferheld

**Supervisor:**

Torsten Berning  
Chungen Yin

**Pages: 73**

**Appendices: 1**

**Project deadline: 01-06-2018**

**Abstract:**

An air-cooled proton-exchange membrane (PEM) fuel cell is used for powering a hydrogen-powered car constructed by Team Aalborg Energy. An open cathode configuration supplies oxygen for the chemical reaction and removes excess heat due to irreversibilities. Flow uniformity through the PEM fuel cell stack is essential for obtaining high fuel cell efficiency. This thesis investigated the current manifold design, with the help of computational fluid dynamics (CFD). A porous media approach was used to reduce the number of cells and computational time. Results showed a highly uniform flow through the fuel cell stack, with less than 5% difference in flow velocity from the center to the outer part of the stack. Leading to an evenly distributed temperature throughout the entire stack. Numerical investigations showed that blowing air through the stack was less efficient, compared to creating a suction effect at the outlet of the fuel cell stack.



# Preface

---

This master thesis project report has been made during the 4<sup>th</sup> semester on the Thermal Energy and Process Engineering M.Sc. program at Aalborg University.

## Reading guide

Throughout the report all references are listed by the end of the project report, in the bibliography. The references are denounced cf. the Harvard method, hence a statement will be referred by [Surname, year]. If more than one reference from the same year has the same author, these are denoted with a, b, c and so forth. This reference refers to the bibliography where books are referred by author, title, ISBN-number, publisher, edition and year while websites are referred by author, title, year and URL. Technical papers are referred by author, title and year. Figures, tables and equations are numbered according to the particular chapter they are placed in. The first figure in chapter three will here-fore be assigned with figure number 3.1 and the second 3.2 etc. Descriptive captions for tables are found above relevant tables and captions for figures are found under relevant figures.

## Acknowledgements

The author would like to thanks Xin Gao for guidance and corporation doing the project period. Xin Gao helped with practical as well as numerical issues encountered doing the project.

Aalborg University, June 1, 2018



---

*Stig Eitel Seiferheld*



## Executive summary

---

The work presented in this report originates from years of being a member of a group of students, dedicating their leisure time to building a hydrogen-powered car. Engineering students from different fields of study contribute with knowledge about their own field. In that context, the flow field distribution of the manifold configuration of a proton-exchange membrane (PEM) fuel cell has been investigated.

The purpose of this project was to numerically model the flow field characteristics of the PEM fuel cell used for powering the car. The fuel cell works with a dead-end anode and an open cathode configuration. Meaning that the flow through the cathode is for supplying oxygen for the chemical reaction, as well as removing excess heat produced due to irreversibilities.

Computational fluid dynamics has been used for analysing the heat and flow distribution of the PEM fuel cell. A figure showing the PEM fuel cell and the manifold can be seen in figure 0.1 where the flow direction are indicated.

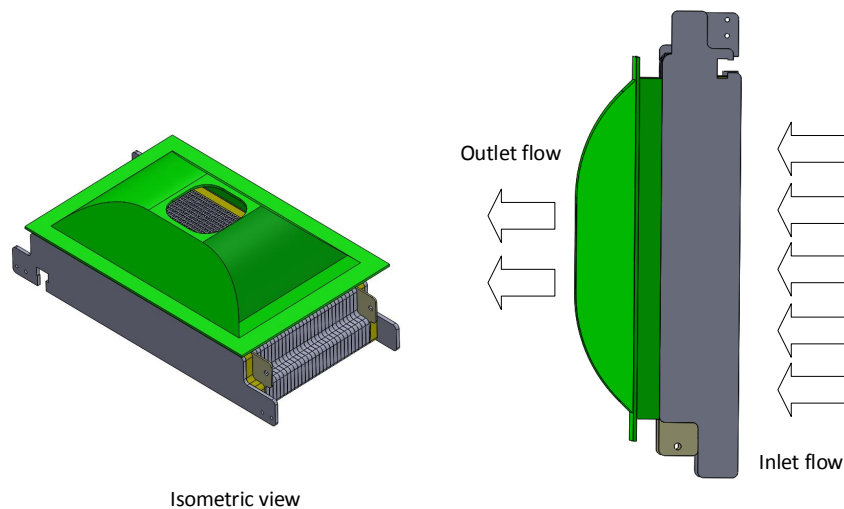


**Figure 0.1:** Figure showing the geometry of the manifold and stack of a Mark1020, PEM fuel cell. With the flow direction indicated

The PEM fuel cell stack has been modelled using a porous media approach. A porous media approach significantly reduces the number of cells (control volumes) used for the numerical modelling. The porous media are modelled by the addition of a momentum source term to the standard fluid flow equations. The source term is composed of two parts: a viscous and an inertial loss term.

Pressure loss coefficients have been determined based on empirically determined pressure losses for the PEM fuel cell stack and corresponding superficial velocities.

Heat transfer through the porous media has been modelled using a non-equilibrium approach, meaning that the fluid and solid (stack) are not in thermal equilibrium. To simulate the heat released within the stack due to irreversibilities, an energy source term has been determined based on the actual cell voltage of the stack which is highly coupled with the current density of the stack.

The numerical results showed great uniformity for the flow through the current manifold configuration. The velocity magnitude from the center towards the ends differed with no more than a maximum of 5%. As a consequence of highly uniform flow, the temperature difference across the stack where highly uniform and increased in the flow direction having its highest temperature at the outlet of the stack.

A parametric study where conducted to see the effect of changing different input parameters. An increasing inlet temperature increased the overall stack temperature, meaning that the stack where operating away from the optimal temperature and thereby decreasing the stack efficiency. Varying the inlet stoichiometry and keeping the inlet temperature constant, showed that it could be beneficial to actually increase the inlet temperature for higher currents due to the fact that higher currents have a higher optimal temperature.

An axial fan is pulling air through the stack, comparing the fan curve with the system pressure drop as a function of required flow rate, showed that for operating currents higher than 30 amps fuel cell performance would decrease since the only way the fan would be able to supply enough flow rate would be by lowering the stoichiometry.

# Contents

---

<b>Nomenclature</b>	<b>XI</b>
<b>1 Introduction</b>	<b>1</b>
1.1 Proton-exchange membrane fuel cell . . . . .	2
1.2 Literature review . . . . .	13
1.3 Introduction to the framework of this project . . . . .	15
<b>2 Problem statement</b>	<b>17</b>
2.1 Motivation . . . . .	17
<b>3 Modelling methodologies</b>	<b>19</b>
3.1 Computation Fluid Dynamics (CFD) . . . . .	19
3.2 Geometrical considerations . . . . .	21
3.3 Meshing methodology . . . . .	23
3.4 Material properties and boundary conditions . . . . .	30
3.5 Energy equation considerations . . . . .	34
3.6 Momentum equation - considerations . . . . .	37
3.7 Solution method . . . . .	40
3.8 Grid independence study . . . . .	42
<b>4 Model validation</b>	<b>47</b>
4.1 Energy and mass balance . . . . .	48
<b>5 Numerical results and discussion</b>	<b>51</b>
5.1 Numerical results . . . . .	51
<b>6 Parametric study</b>	<b>57</b>
<b>7 Discussion</b>	<b>61</b>
7.1 Flow direction . . . . .	63
7.2 Low flow velocity . . . . .	64
7.3 Hub blockage . . . . .	65
7.4 Manifold geometry . . . . .	66
<b>8 Conclusions</b>	<b>67</b>
<b>9 Future work</b>	<b>69</b>
<b>Bibliography</b>	<b>71</b>
<b>A Appendix: Uploaded material</b>	<b>73</b>



## Nomenclature

---

The following list of symbols used in the report, are outlined in the order; lower- and upper case arabic notation, greek notation and the abbreviations.

Symbol	Description	SI-unit
$h_f$	Heat of formation	$kJ \cdot mol^{-1}$
$W_{elec}$	Electrical work	$J \cdot mol^{-1}$
$E$	Voltage potential	V
$F$	Faraday constant	$C \cdot mol^{-1}$
$\Delta G$	Gibbs free energy	$kJ$
$R$	Gas constant	$J \cdot K^{-1}mol^{-1}$
$T$	Temperature	K
$\dot{N}$	Consumption rate	$mol \cdot s^{-1}$
$I$	Current	A
$\dot{m}$	Mass flow rate	$kg \cdot s^{-1}$
$\dot{Q}$	Heat flow	W
$C_p$	Specific heat	$J \cdot kg^{-1}K^{-1}$
$i$	Current density	$A \cdot m^{-2}$
$R$	Ohmic resistance	$\Omega$
$\eta$	Efficiency	-
$\rho$	Density	$kg \cdot m^{-3}$
$k$	Thermal conductivity	$W \cdot m^{-1}K^{-1}$
$\mu$	Dynamic viscosity	$kg \cdot m^{-1}s^{-1}$
$A$	Area	$m^2$
$P$	Pressure	Pa
$V$	Volume	$m^3$
$n$	Mole	mole
$m$	Mass	kg
$\zeta$	Stoichiometry	-
$\gamma$	Porosity	-
$v$	Velocity	$m \cdot s^{-1}$
$h$	Heat transfer coefficient	$W \cdot m^{-2}K^{-1}$

Abbreviation	Description
PEM	Proton-exchange membrane
CFD	Computational fluid dynamics
3D	three-dimensional
2D	two-dimensional



# Introduction

# 1

Since 2013, Team Aalborg Energy has been competing in the annual Shell Eco-Marathon, an event hosted by Shell. Shell Eco-Marathon is one of the world's leading energy efficiency competition programmes. The competition challenges students all around the world to design, build and drive the most energy-efficient car. Pushing the boundaries of what is technically possible. The students take their designs to the track in the annual Mileage Challenge to see which vehicle can compete to go the farthest on least amount of fuel [Shell, 2018].

The Shell Eco-Marathon is held once a year, in Asia, America, and Europe, with the competition in Europe being the absolute biggest. The best teams from the competition in Asia and America are invited to participate in the Shell Eco-Marathon in Europe. There are two main categories at the Shell Eco-Marathon, the Urban Concept and the Prototypes. Team Aalborg Energy, is competing in the Urban Concept category with their car *Cimbrer II*, seen in figure 1.1.



**Figure 1.1:** Team Aalborg Energys car Cimbrer II that has competed in the Shell Eco-Marathon since 2017.

The cars in the Urban Concept category is divided into groups depending on their propulsion system. Team Aalborg Energy is a part of the *hydrogen* category, being the absolute largest category for the Urban Concept vehicle. In 2015, Team Aalborg Energy set the currently best record attempt leading to a 3rd place in the competition with a fuel consumption of  $204.2 \frac{\text{km}}{\text{m}^3}$  of hydrogen which is equivalent to approximately  $640 \frac{\text{km}}{\text{L}}$  of petrol.

Students from different semesters and specialisations collaborate in designing, building and developing *Cimbrer* further. This means that there are several working areas on the car. From motor control, mechanical construction, aerodynamics to fuel cell performance. All these can be investigated to see whether it is possible to improve the efficiency of the overall system.

## 1.1 Proton-exchange membrane fuel cell

*In this project, focus will be on the main source of energy for the car, the fuel cell, all the electricity that the car consumes for the motors, lights and onboard electronics is produced by the fuel cell. The references of this section are based on a textbook by [Barbir, 2005].*

A fuel cell is an electrochemical energy converter, that converts the chemical energy of a fuel, in this case, hydrogen, directly into electrical energy. Different types of fuel cells exist and are distinguished by the electrolyte used. The fuel cell used in *Cimbrer II*, is a Mark1020 Proton-exchange membrane (PEM) fuel cell from Ballard, consisting of 28 cells. Therefore focus will be on this type of fuel cell.

The proton-exchange membrane got its name due to the unique capabilities of the polymer membrane at the center of the cell. As the name suggests, the proton-exchange membrane is able to conduct protons but is impermeable to gasses. The membrane acts as an electrolyte and is sandwiched between two porous electrically conductive electrodes. Between the porous electrodes and the membrane is a catalyst layer, which enhances the chemical reactions. Finally, the cell is composed of bipolar plates on each side of the membrane where hydrogen and oxygen is feed in respectively, the can be seen in figure 1.2.

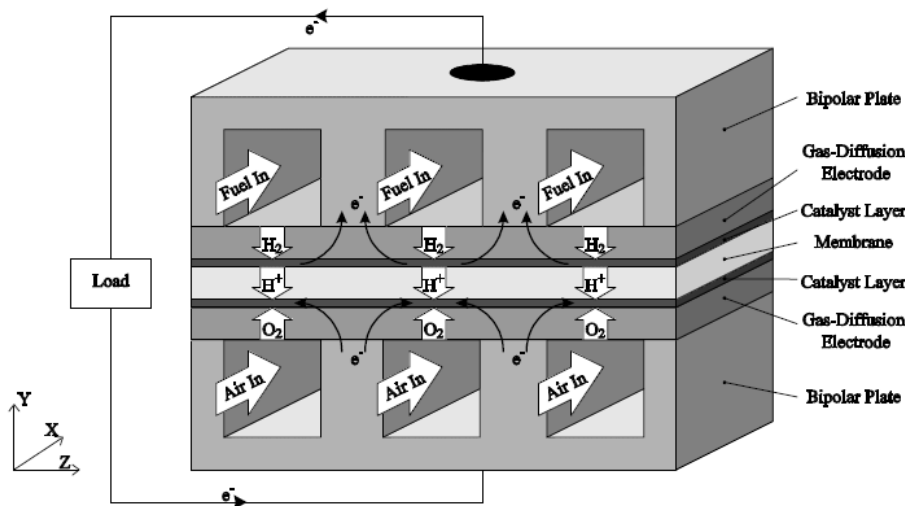


**Figure 1.2:** Figure showing the structure of the cell [Berning, 1997].

### 1.1.1 PEM operating principle

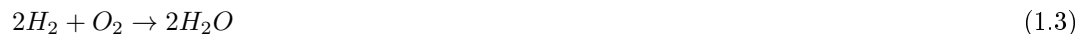
The operating principle of the PEM fuel cell is easiest shown using the chemical reactions occurring at the anode and cathode side of the cell. The electrochemical reaction happens at the interface between the catalyst layer and the electrolyte membrane. Hydrogen is fed in on one side of the membrane, hydrogen diffuses through the gas diffusion layer and as it reaches the catalyst layer it is split into its primary components - electrons and protons. Each hydrogen molecule consists of two protons and two electrons according to equation 1.1.



The protons are able to transit through the membrane, where the electrons travel through the conductive electrodes and an electrical circuit producing electrical work before coming back to the other side of the membrane. At the catalyst layer on the other side of the membrane, the electrons meet up with the protons that migrated through the membrane and oxygen diffusing through the other diffusive layer. A new chemical reaction occurs and water is formed. The water is pushed out of the cell and removed due to an excess flow of oxygen. The chemical reaction of this side can be described according to equation 1.2.



The results of these chemical reactions is a current of electrons flowing through an external circuit - direct electrical current. The side where hydrogen is fed in is referred to as the anode side. While the side where oxygen is fed into the cell is referred to as the cathode side. The overall reaction can, therefore, be described according to equation 1.3.



The described reactions may contain several intermediate reactions, but these are not relevant for this thesis.

### 1.1.2 PEM fuel cell thermodynamics

The reaction presented by equation 1.3 is the combustion of hydrogen. Combustion is an exothermic process, meaning that heat is released. The amount of energy absorbed or evolved when one mole of the product is formed from a chemical reaction at 298 K and 101.3 kPa can be calculated from the difference in the sum of the heat of formations of both the products and reactants [Schaschke, 2014]. For the combustion of hydrogen, we can, therefore, write the following equation 1.4.



The heat of formation of liquid water is  $-286\text{kJmol}^{-1}$ , while the heat of formation of elements by definition is zero. The heat released from hydrogen combustion can, therefore, be described as equation 1.5.

$$\Delta H = (h_f)_{H_2O} - (h_f)_{H_2} - 1/2(h_f)_{O_2} = -286\text{kJmol}^{-1} \quad (1.5)$$

The negative sign for the enthalpy means that the reaction, by convention is releasing heat, meaning that the chemical reaction happening inside the fuel cell is exothermic.

The enthalpy from the hydrogen reaction is often referred to as the heating value of hydrogen and is the heat released by a complete combustion of 1 mole of hydrogen. We distinguish between two different heating values, the higher- and lower-heating value. The measurement of heating values is conducted using an enclosed calorimetric bomb where hydrogen is fully combusted with oxygen. In the case where the products ( $H_2O$ ) is in a vapour phase as for most combustions, the lower-heating value is found. That means that less heat is released from the combustion. The lower-heating value of hydrogen is  $-241\text{kJmol}^{-1}$ . Therefore the difference between the higher and lower heating value is simply the heat of evaporation of water.

### 1.1.3 Theoretical cell potential

The heating value of hydrogen is a measure of the maximum potential energy output for the fuel cell. It is the maximum *thermal* energy available. But the energy produced in a fuel cell is in terms of electrical work, therefore the question is whether it is possible to convert all our potential thermal energy of hydrogen into electrical potential energy. This would be possible if and only if the entropy change  $\Delta S$  is zero. This is not the case and therefore some of hydrogen's higher heating value cannot be converted into useful electrical work. However, the amount that can correspond to Gibbs free energy and can be represented by the following equation 1.6.

$$\Delta G = \Delta H - T\Delta S \quad (1.6)$$

This means that there are some irreversible losses in the electrochemical energy conversion due to the creation of entropy,  $\Delta S$ . As for the  $\Delta H$ , the difference in entropy is calculated as the difference between the entropies of the products and reactants as in equation 1.7.

$$\Delta S = (s_f)_{H_2O} - (s_f)_{H_2} - 1/2(s_f)_{O_2} \quad (1.7)$$

The entropies for the products and reactants at 298 K and 101.3 kPa can be seen in table 1.1.

**Table 1.1:** The entropies of the products and reactants for the fuel cell reaction at standard conditions [Barbir, 2005].

	$s_f(kJmol^{-1}K^{-1})$
Hydrogen, $H_2$	0.13066
Oxygen, $O_2$	0.20517
Water (liquid), $H_2O$ (l)	0.06996
Water (vapour), $H_2O$ (g)	0.18884

Based on the numbers in table 1.1, and the number calculated in equation 1.5 ( $286kJmol^{-1}$ ). The amount of energy that may be converted into electrical energy is  $237.3kJmol^{-1}$  while the remaining  $48.7kJmol^{-1}$  is converted into heat. As mentioned, this is only for temperatures of 298 K, and with the product water in liquid form. For other temperatures, these values will be different.

However this is still in terms of  $kJmol^{-1}$ , and not as an electric potential. What we can do is to recall that electric work is the product of potential and charge as in equation 1.8

$$W_{elec} = qE \quad (1.8)$$

Where,  $W_{elec}$  is the electrical work in  $Jmol^{-1}$ ,  $q$  is charge in *Coulombs mol<sup>-1</sup>* and  $E$  is the potential in *Volts*.

The total charge of the fuel cell reaction, can be calculated as the product of the number of electrons per molecule of hydrogen  $n$ , multiplied by the number of molecules per mole also known as the Avogadro number ( $6.002 \times 10^{23}$ ) and the electronic charge of one electron ( $1.602 \times 10^{-19}$ ). The product between the charge of one electron and the Avogadro number is also known as the Faraday constant ( $96485C/mole$ ). The total charge can, therefore, be written as equation 1.9

$$q = nF \quad (1.9)$$

Which if combined with equation 1.8, gives the electrical work expressed as equation 1.10

$$W_{elec} = nFE \quad (1.10)$$

Where the maximum amount of electrical energy that can be generated in a fuel cell, corresponds to the Gibbs free energy,  $\Delta G$ . Combining this with equation 1.10 gives the following expression for the theoretical cell potential.

$$E = \frac{-\Delta G}{nF} \quad (1.11)$$

Using the result from the calculation in equation, 1.6 gives a theoretical cell potential of 1.23 V. This is at a temperature of 298 K and is also known as the cell potential under standard conditions. The reaction does not always happen at standard conditions and for such cases the Nernst equation has been derived. Having knowledge about the composition of the electrochemical reaction allows the determination of the cell potential at other than standard conditions. And can be described by the Gibbs free energy in equation 1.12.

$$\Delta G = \Delta G^\circ + RT \ln Q \quad (1.12)$$

As for any chemical reaction of:



When the reaction is at equilibrium it is possible to determine an equilibrium constant  $K$ , however this mathematical expression also holds for situations where the system is not at equilibrium but where the composition is known, in this case, the constant is referred to as  $Q$ . It is important to note that this is not an equilibrium constant like  $K$ .  $R$  is the universal gas constant and  $T$  is temperature. Combining this with the expression from equation 1.11 gives the following expression:

$$-nFE = -nFE^\circ + RT \ln Q \quad (1.14)$$

Which can be rearranged into the following expression for the cell potential at nonstandard conditions:

$$E = E^\circ - \frac{RT}{nF} \ln Q \quad (1.15)$$

This function is still depended on temperature. The effect of temperature on the free energy change can be calculated from equation 1.6 as [of Arizona]:

$$\frac{\partial G}{\partial T}_p = -\Delta S^\circ \quad (1.16)$$

Introducing this in equation 1.15, gives the following expression for the cell potential [Berning, 1997]:

$$E = E^\circ - \frac{\Delta S^\circ}{2F}(T - T^\circ) - \frac{RT}{nF} \ln Q \quad (1.17)$$

### 1.1.4 Fuel cell anode and cathode configuration

The PEM fuel cell inside the car operates with a dead-end anode open cathode configuration. Operating the fuel cell anode with a dead-end configuration requires a pressure regulator that regulates the supply pressure down to the required anode pressure [Ballard, 2011]. Operating the anode in the dead-end configuration requires very pure hydrogen. Since the hydrogen supplied is never 100% pure, impurities will accumulate at the anode side and eventually decrease the fuel cell performance. Also a build-up of nitrogen crosses over from the cathode side. In order to solve this problem, the fuel cell is purged regularly with a purge valve to remove the impurities and increase the hydrogen fraction at the anode side. The anode side configuration can be seen in figure 1.3.

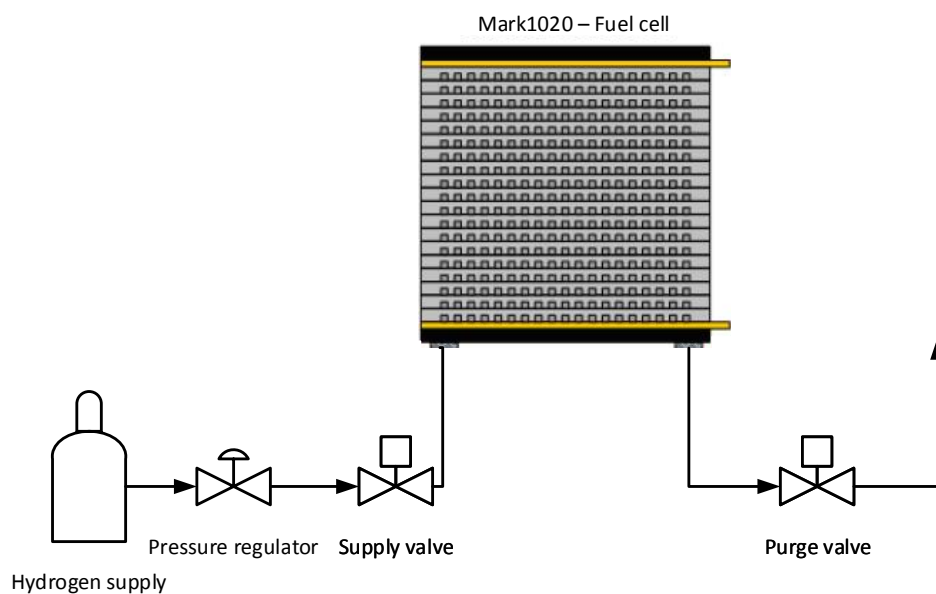


**Figure 1.3:** Figure showing the anode configuration in dead-end mode, [Ballard, 2011].

The open cathode configuration means that the cathode is open to the surroundings. There are two main purposes of the open cathode configuration, one is to provide the required amount of oxidant that the fuel cell needs for the reaction presented in equation 1.3. And second and lastly to provide coolant for the stack. Stack operations result in the production of waste heat that needs to be removed in order to maintain the stack at the proper temperature. The heat rejected from the stack is removed by the air flowing through the open cathode.

Therefore the air flow rate at the cathode can be broken into two different parts, the *oxidant specification*, which specifies the amount of air need for the stack operation (the chemical reaction). And the *coolant specification*, which specified the required airflow to remove the waste heat from the stack and keep it at the proper temperature.

The required air flow rate at the inlet of the cathode has to be equal to or higher than the rate at which the reactants are consumed at the fuel cell. The rates in  $mol/s$  at which the oxygen is being

consumed, can be determined based on Faraday's law [Barbir, 2005]:

$$\dot{N}_{O_2} = \frac{I}{n_e F} \quad (1.18)$$

Where  $\dot{N}_{O_2}$ , is the consumption rate ( $mols^{-1}$ ),  $I$  is current (A),  $n_e$  is the number of electrons per mole of oxygen and  $F$  is Faraday's constant. This can be represented on a mass consumption rate, by multiplying by the molar mass  $M_{O_2}$  of oxygen. Furthermore, multiplying the equation by the number of cells  $n$  in the stack (28) gives the opportunity of determining the required oxygen flow rate based on the stack current:

$$\dot{m}_{O_2} = \frac{I}{n_e F} M_{O_2} n_{cell} \quad (1.19)$$

Since the flow through the open cathode is not pure oxygen but air, a correlation is needed. Air contains approximately 21% of oxygen [Ballard, 2011], therefore, the equation can be rewritten as:

$$\dot{m}_{air} = \frac{I}{n_e F} \frac{1}{0.21} M_{air} n \quad (1.20)$$

In most situations, the coolant flow rate far exceeds the oxidant flow rate, therefore the coolant flow rate is often used as the design parameter. However, to determine coolant flow rate, information about the stack heat generation is needed. As will be addressed in the following subsection 1.1.5

### 1.1.5 Stack heat generation

In order for the stack to maintain the desired stack temperature, the heat generated as a by-product of the electrochemical reaction needs to be removed from the stack. Having information about the heat generation of the stack is an important design parameter when determining the coolant flow rate. In order to determine the stack heat generation, an energy balance for the fuel cell stack is needed. As mentioned in 1.1.2 on page 3, hydrogen has a higher and lower heating value, where the higher heating value is used when the products is in a liquid state. However, the products ( $H_2O$ ) is in a vapour state in a fuel cell. Therefore it is more appropriate to use the lower heating value, to determine the thermal energy released.

As mentioned by the Gibbs free energy, not all the thermal energy can be converted into electrical energy and there will be some heat loss due to irreversibility. Therefore the following energy balance can be written:

$$\frac{I}{n_{e,H_2} F} H_{LHV} n_{cell} = \dot{Q}_{heat} + IV_{cell} n_{cell} \quad (1.21)$$

Where  $n_{e,H_2}$  is the number of electrons per mole of hydrogen. This expression can be rearranged to find the heat generated inside the stack as:

$$\dot{Q}_{heat} = (1.254V - V_{cell})In_{cell} \quad (1.22)$$

This, however, is just a good approximation of the stack energy balance. A complete stack energy balance would have to take the heat (enthalpy) brought into the stack by the reactants, unused heat of reactant gasses leaving the stack and heat dissipated to the surroundings. This equation is, however, the same as [Ballard, 2011] uses for determination of the required coolant mass flow rate. Since the heat removed by the air can be calculated as [Ballard, 2011]:

$$\dot{Q}_{removed} = (T_{inlet} - T_{outlet})\dot{m}C_p \quad (1.23)$$

Where  $T_{inlet}$  is the inlet air temperature,  $T_{outlet}$  is the outlet air temperature and  $C_p$  is the specific heat capacity of air.

### 1.1.6 Polarization curve

The theoretical cell potential as mentioned in 1.1.3 on page 4 could be predicted using the Nernst equation, which corresponds to an equilibrium (open circuit) state [Berning, 1997]. However, the actual cell potential is different from the theoretical cell potential, usually less than 1V [Barbir, 2005]. When the electrical circuit is closed with a load and a current is generated, the potential of the cell will drop even further as a function of the current being generated. This is due to unavoidable losses, mainly known as the activation-, ohmic-, and mass transport losses.

#### Activation losses

Some voltage difference is needed from the equilibrium to get the electrochemical reaction going, this is called the activation polarization losses. It is due to the slow reactions taking place at the surface of the electrodes and happens for both the anode and cathode side. However, oxygen reduction requires much higher overpotentials, compared to the oxidation of hydrogen [Barbir, 2005]. For a PEM fuel cell the overpotential can be described by the Tafel equation:

$$\eta_{act} = b \ln \frac{i}{i_o} \quad (1.24)$$

Here  $b$ , is the Tafel-slope,  $i$  is the current density and  $i_o$  is the exchange current density. The exchange current density is a measure of the electrodes willingness to proceed with the electrochemical reaction. The higher the exchange current density the lower the activation losses.

#### Ohmic losses

Ohmic losses are due to the resistance to the flow of ions in the electrolyte and due to electrical resistance in the electrodes. And can be expressed by Ohms law [Barbir, 2005]:

$$\eta_{ohm} = iR_i \quad (1.25)$$

Where  $R_i$  is the total internal resistance. The ohmic losses can be reduced by lowering the thickness of the electrolyte, however, this may lead to higher diffusion of hydrogen through the electrolyte.

### Mass transport losses

The concentration of the reactants at the surface of the catalyst depends on the current density. The higher the current density, the lower the surface concentration. At some point the concentration at the surfaces reaches zero, that is when the rate of consumption of reactants becomes equal to the amount of reactants that can be supplied due to diffusion. The current density at which this happens is known as the limiting current density. The fuel cell cannot produce more than the limiting current density since there are no reactants at the catalyst surface [Barbir, 2005]. The voltage drop due to mass transport or concentration losses can be obtained from:

$$\eta_{mass} = \frac{RT}{nF} \ln \left( \frac{i_L}{i_L - i} \right) \quad (1.26)$$

Where  $i_L$  is the limiting current density.

Due to nonuniform conditions over the electrode area, this limiting current is almost never experienced in practical fuel cells [Barbir, 2005]. To see such sharp drop in the cell potential, the limiting current would have to be reached over the entire electrode surface at the same instance.

### Internal currents and crossover losses

This may happen at very low current densities or even when the outer circuit is disconnected [Berning, 1997]. The polymer membrane inside the cell is practically impermeable to reactant gasses, however, hydrogen is highly diffusive and some of it will cross the membrane. For each hydrogen molecule that diffuses through the membrane and reacts with oxygen at the cathode side of the cell will result in two fewer electrons in the generated current of electrons going through the external circuit [Barbir, 2005]. Since the rate at which hydrogen diffuses through the membrane is several magnitudes lower than the consumption rate of hydrogen or total electrical current generated, the impact seems small. However, when the fuel cell is at open circuit potential or operating at very low current densities, the losses have a way higher impact. This may be observed in figure 1.4.

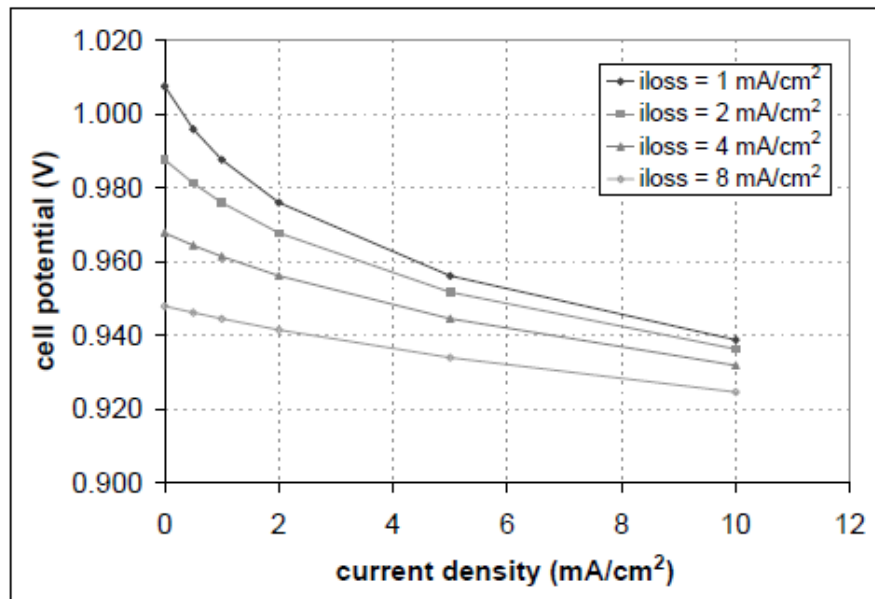


**Figure 1.4:** Figure showing the effect of the internal and/or cross over losses on the open circuit potential [Barbir, 2005].

By combining these losses it is possible to construct what is known as the fuel cell polarization curve. The curve is formed by subtracting the activation-, ohmic- and concentration losses from the equilibrium potential. From the curve, it is possible to determine the actual cell voltage, depending on the current. The polarization curve for the Ballard Mark1020 stack can be seen in figure 1.5. The graph is plotted using an equation for the cell voltage potential as specified in the manual by [Ballard, 2009]:

$$CV = -0.0019 \cdot i^3 + 0.268 \cdot i^2 - 14.34 \cdot i + 973.6 \quad (1.27)$$

Here  $i$  is the stack current, and  $CV$  is the average cell voltage in mV.

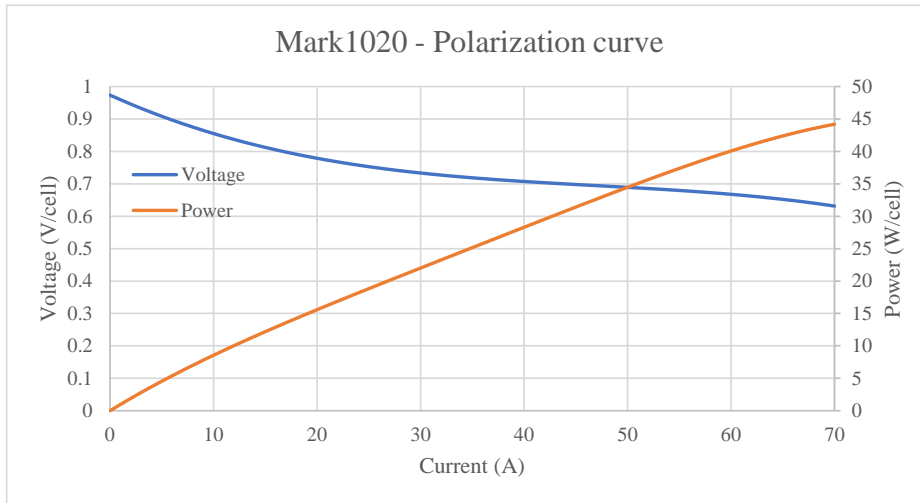


**Figure 1.5:** Figure showing the polarization curve for the Mark1020 fuel cell stack [Ballard, 2009].

### 1.1.7 Theoretical fuel cell efficiency

For an electrochemical energy converter, a fuel cell. The efficiency can be determined as for an energy converting device, simply as the ratio between the energy output and the energy input to the system. In a fuel cell the energy input is the enthalpy of hydrogen, the higher heating value of hydrogen as explained previously. Assuming that the Gibbs free energy can all be converted into electrical energy, makes it possible to calculate the theoretical maximum efficiency of the fuel cell as in equation 1.28

$$\eta = \frac{\Delta G}{\Delta H} = \frac{237.3}{286} = 83\% \quad (1.28)$$

It is convenient to express the fuel cell efficiency using the lower heating value of hydrogen, due to the fact that it results in a higher efficiency. But is also justified due to the fact that the products for a fuel cell is in a vapour state. As mentioned previously at the beginning of subsection 1.1.2 on page 3, the lower heating value of hydrogen is  $241 \text{ kJ mol}^{-1}$ . And recalculating the Gibbs free energy using equation 1.6 gives the following theoretical fuel cell efficiency:

$$\eta = \frac{\Delta G}{\Delta H_{LHV}} = \frac{227.8}{241} = 94.5\% \quad (1.29)$$

## 1.2 Literature review

The purpose of this section is to present a fuel cell modelling literature study. To give a good idea of how to approach the modelling of the fuel cell stack. As mentioned the fuel cell stack used within the car is a Mark1020 PEM fuel cell stack. Therefore focus will mainly be on modelling methodologies used for modelling similar types of fuel cells.

An article by [Macedo-Valencia et al., 2016], used a three-dimensional model to simulate the fluid flow, heat transfer, electrochemical reaction and species transport in a PEM fuel cell stack consisting of five cells, including membrane, gas diffusion layers, catalyst layers, the flow channels and the current collectors. The current densities found from the model corresponded well to that the pulverization curve for the stack. The mesh consisted of 16,000,000 cells to resolve everything and get accurate solutions.

An article by [Choopanya and Yang, 2016], investigates different meshing methodologies for PEM fuel cells to come up with guidelines for how to mesh a PEM fuel cell. Their research shows that for modelling a single channel the normal amount of cells used is approximately  $10^4$  cell elements. The purpose is to find out where the mesh can be more coarse in order to save element and eventually computational time without going down in accuracy. For the study, they use a single cell where the oxygen and hydrogen are separated by the catalyst layers, gas diffusion layers and membrane. The reactants are flowing in an u-form configuration. Their finding shows that the mesh size can be reduced in the axial direction without limiting the accuracy of the solution in a notable range. The axial direction corresponds to the y-direction in figure 1.6.

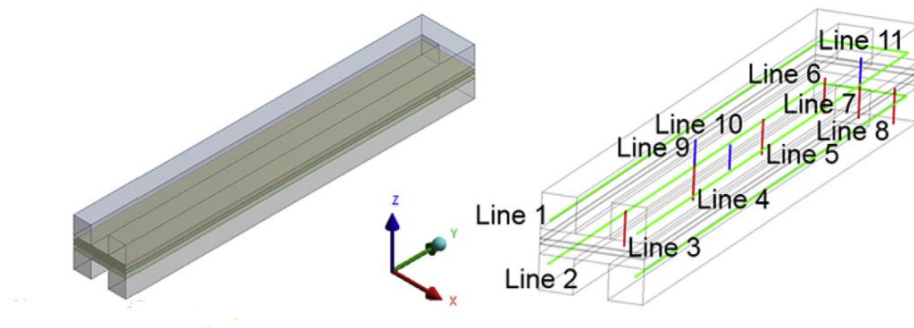


**Figure 1.6:** Figure showing the geometry used for the CFD calculations [Choopanya and Yang, 2016].

An article by [Jithin et al., 2017], investigates the simulation of coupled heat and mass transport for the reaction in a PEM fuel cell at the cathode side using the Boltzmann method. They found that there are two major factors that can improve the fuel cell performance, a higher flow rate of reactants and the effective porous media species diffusion coefficient. They suggested to research for better gas diffusion layers to improve the transport properties of the oxygen. It was found that increasing the flow rate of reactants at higher current densities was more favourable than at lower current densities.

The article by [Wang et al., 2011] reviewed the literature on the flow maldistribution in PEM fuel cell stacks and found that they presented results are unsystematic, scattered or even contradictory. The article highlighted the effects of flow maldistribution on heat and mass transfer in PEM fuel cell stacks. Previous simulations had shown that the removal rate of water vapour in the channels with low velocity, is less which consequently resulted in more earlier and frequently higher occurrence of uniform temperature than in the channels having higher flow velocity. The manifold for a PEM fuel cell stack is either carved into the bipolar plates or placed externally, where the externally manifold was cheaper. When the flow is parallel, the configurations where either U-type (reverse flow) or a Z-type (parallel flow) in the literature. It was concluded that the flow distribution in a parallel configuration usually can be influenced by the geometrical design.

Another article by [Mohan et al., 2004], models the hydrogen and air maldistributions between cells of a PEM fuel cell stack. The model was solved using Ansys Fluent, to reduce the computational time the flow resistance (pressure drop) of some of the channels were specified as a porous media with a flow resistance coefficient determined experimentally. The simulations showed that flow rate and port size has a great influence on the maldistribution of the fluids, which can be considerably skewed if a larger number of cells are stacked together.

In an article by [Jeong et al., 2013], a 3D-CFD simulation was developed to simulate the flow through the manifold and to optimize the shape. The author emphasised that to resolve the channels of a PEM fuel cell stack hundreds of thousands of cells have to be generated. To reduce computational time and reduce the number of cells, the author used a porous media approach simplifying the more complex channel geometry by straight channels with a specified resistance coefficient determined by the Darcy-Forchheimer equation. The coefficients were found by experimentally measuring the pressure drop through a single cell as a function of velocity. The simplification of the geometry can be seen in figure 1.7.

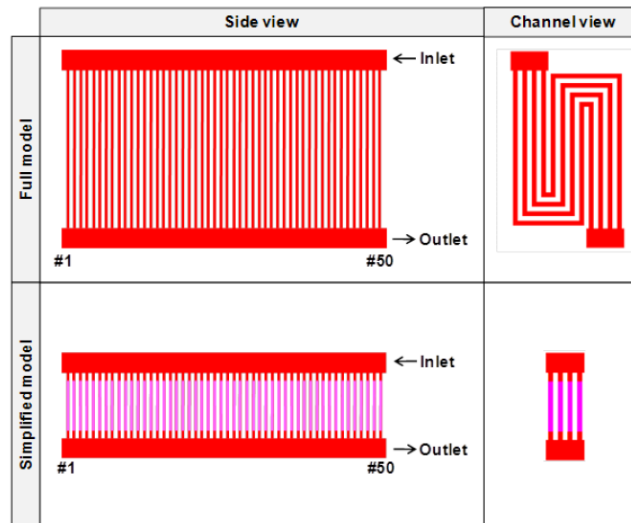


**Figure 1.7:** Comparison of the simplified and original configuration [Jeong et al., 2013].

The number of cells used for the full model was 1,682,424 number of cells. While the simplified model used no more than 396,024 number of cells. The results of the full-scale model, where compared with those of the simplified one to verify the integrity of the simplified model. Conclusively it was determined that the results of the simplified model more than satisfactorily represented those of the full model. [Jeong et al., 2013] discovered that the size of the manifold significantly influenced the uniformity of the flow between the cells, and the optimal manifold size was found for a 30kW stack.

An article composed at Aalborg university by [Gao et al.] investigates the flow and consequently heat distribution of a low temperature PEM fuel cell stack from Ballard. Throughout the project, a porous media approach was used to represent the cells of the fuel cell stack. The model was validated by comparing the pressure losses from the model with those experimentally determined and showed good coherence. The CFD simulations showed that cavities in the manifold design induced swirl at the edges of the stack outlet. After sealing these cavities a far more even temperature distribution was experienced at the surface of the fuel cell stack. It was concluded that by sealing both the cavities in the manifold design, the uniformity of the flow was increased by about 72%. Furthermore, before the stack inlet, an air filter is placed. The modelling methodology for the filter is the same as for the stack, using a porous media approach with specified loss coefficients (pressure). A spacing between the filter and stack inlet exist, and simulations using fins between these showed to be able to improve the flow uniformity by around 4% meaning that the total uniformity improvement is 76% utilising sealings and fins.

### 1.3 Introduction to the framework of this project

Some of the basics surrounding the operation of PEM fuel cells have been described, and will be utilised for the framework of this project. Throughout the state of the art literature study, and examination of current research regarding experimental but mostly numerical work has been conducted. The examination showed, that several numerical methods can be utilised to describe everything from flow distribution, temperature distribution to current densities. Eventually, all these finding showed that the uniformity of the flow rate plays an important role for the heat transfer and current density distribution. Most of the models that included species transport, where validated based on the current density of the model compared to those specified by the manufactures polarisation curve. However the simulations of entire cells showed to use a comprehensive amount of cells for refinement. A way to solve this problem is by simulating the stack as a porous media with specified pressure losses. The pressure loss and coefficients were determined based on experimental work. Most of the CFD simulations conducted where based on ANSYS Fluent. Many articles investigated the manifold shape and its contribution to non or uniformity in the flow. Therefore the objective of this thesis will be to investigate the flow distribution of the current manifold set-up used for the Ballard 1020 stack inside the car *Cimbrer II*. Based on the literature study, a simplification of the stack is possible with the porous media approach, therefore this thesis will use a similar methodology to reduce the number of required cells and computational time needed. A numerical model will be constructed to predict the flow distribution for the current manifold design. Validating the model will be based on similar approaches to those presented in the state of the art, regarding pressure and temperature distribution. The current manifold design and placement can be seen in figure 1.8 on the next page. Where the flow direction for the current manifold is highlighted.

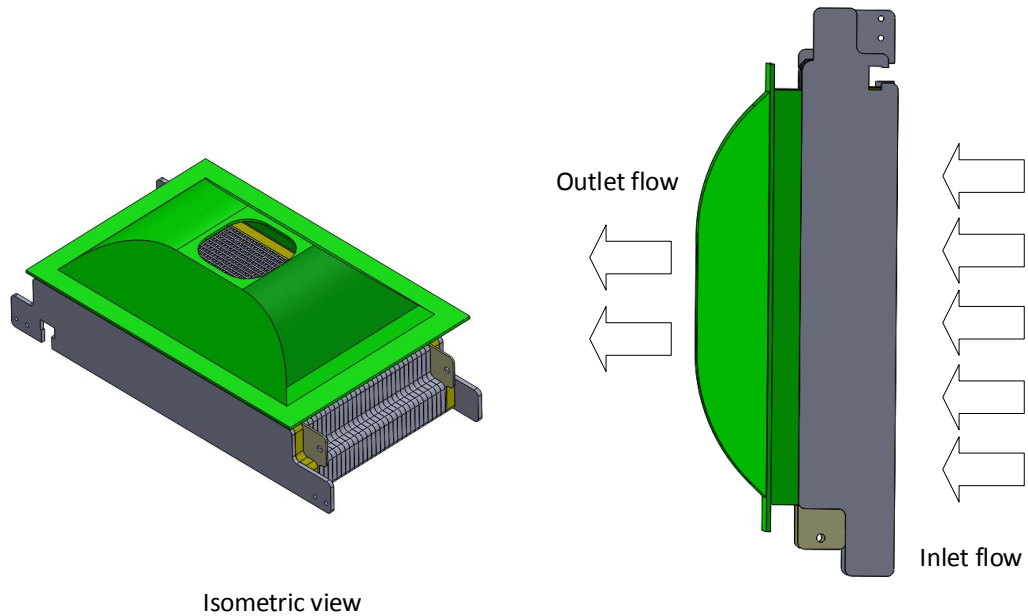


**Figure 1.8:** Figure showing the geometry of the manifold and stack of a Mark1020, PEM fuel cell.

The geometry shown in figure 1.8, is a 1:1 full scale CAD-drawing constructed using Solidworks2015. This geometry will be simplified for modelling purposes, one being representing all the cooling channels which can be seen through the hole at the top of the manifold where the axial-fan is located, using a porous media approach. The open cathode configuration means, that air is being sucked through the stack. Therefore the inlet flow is at the bottom of the stack that is depicted in the figure. The above forms basic for a problem statement, which can be seen in chapter 2.

## Problem statement

---

# 2

*Based on the topics covered in the preceding text, this chapter outlines the objectives of this project.*

The main objective of this thesis, will be to numerically investigate the flow characteristics of the current manifold configuration used for the Ballard Mark1020 - PEM fuel cell stack used for the hydrogen powered car Cimbrier II. As mentioned in 1.2 on page 13 a porous media approach can be used to significantly reduce the number of cells.

Furthermore, a model validation will be done based on experimental results to insure model integrity.

To form a basis for solving this problem the following research questions will be answered throughout this study:

1. How can the flow distribution of the Mark1020 PEM fuel cell stack be described?
2. What effect does the geometry shape of the manifold have of the flow distribution?
3. What is the effect of placing the fan upstream or downstream?

### 2.1 Motivation

Since I first discovered Team Aalborg Energy doing my 4th semester as a bachelor student, I have been heavily involved within this free organisation of students dedicating their leisure time to design, build and develop an hydrogen powered car. Using the knowledge acquired throughout the education, to further develop our engineering skills. Working on this car project gave me and my fellow students unique opportunities to work with and solve real case engineering problems. Since joining the team in 2015 I have been representing Aalborg University in one of the biggest mileage challenges in the world in Rotterdam, and London. I was the pilot of the car, when we set our currently best mileage attempt so far in 2015 in Rotterdam of approximately  $640\text{km/L}$ .

Furthermore with the help of one of my fellow students I have been responsible of designing the new aerodynamic shell of the car *CimbrierII*, that has been racing on the streets of London last year in 2017, where minor technical difficulties were the only reason for not beating our previously best attempt.

It has been a huge honour for me to represent the team at several occasions doing my studies, including featuring on live regional television in Northern Jutland. Peaking with the presentation of *CimbrierII* for His Royal Highness Prince Joachim, in 2017 at Denmark's Technical University - DTU.

Therefore it was only natural for me to do one final project related to the car. This project will deal with the flow and heat distribution of the current fuel cell stack and manifold configuration. The purpose is to construction a three-dimensional (3D) computational fluid dynamics (CFD) model to investigate the flow and heat distribution to try and further optimise the manifold shape for a more uniform flow distribution throughout the stack. Hopefully the results of this project will help the team beating our current record when *CimbrerII* is racing the streets of London yet again in the beginning of July this year.

It is important, that the report structure is ordered in such way that it is possible for new and current team members to use the modelling methodology and results for further optimisation.

This chapter presents the modelling methodologies used to model the flow distribution of the Mark1020 fuel cell stack from Ballard, used for Team Aalborg Energy's car Cimbrer II. Throughout this chapter, the geometry used will be presented, together with a meshing methodology. The determination of boundary conditions and source terms will be presented. Furthermore, a grid independence study will be conducted to ensure that the finalised mesh is of sufficient quality to resolve the solution accurately.

## 3.1 Computation Fluid Dynamics (CFD)

Computational fluid dynamics is used for analysing systems involving fluid dynamics and fluid mechanics problems and if used correctly, CFD is a very powerful tool. The method can be based on several different numerical schemes, however, for this project ANSYS Fluent have been utilised which build on the finite volume method (FVM) [Versteeg and Malalasekera, 2007].

The method seeks to solve the governing equations of fluid dynamics. The equations represent mathematical statements of the *conservation laws of physics*:

- The fluid mass is conserved
- The rate of change of momentum equals the sum of forces acting on a fluid particle (Newton's second law)
- The rate of change of energy equals the sum of the rate of heat addition and the rate of work done on a fluid particle (first law of thermodynamics)

These can be represented by the general transport equation 3.1. Here  $\phi$  represent any arbitrary property like e.g. a pressure component which is conserved and described within a finite control volume (CV) [Versteeg and Malalasekera, 2007].

$$\underbrace{\frac{\partial(\rho\phi)}{\partial t}}_{\text{Transient-}} + \underbrace{\text{div}(\rho\phi\mathbf{U})}_{\text{convective-}} = \underbrace{\text{div}(\Gamma\nabla\phi)}_{\text{diffusive-}} + \underbrace{S_\phi}_{\text{source-term}} \quad (3.1)$$

Here  $\rho$  represent the density of the fluid, while  $\mathbf{U}$  is the velocity of the fluid,  $\Gamma$  represents the diffusion coefficient, such as mass diffusivity for particle motion,  $\nabla$  is the gradient, while  $div$  represents the divergence [Tu et al., 2007].

A typical CFD code project consists of three main elements: A pre-processor, a solver and a post-processor this is represented with the flowchart in figure 3.2.

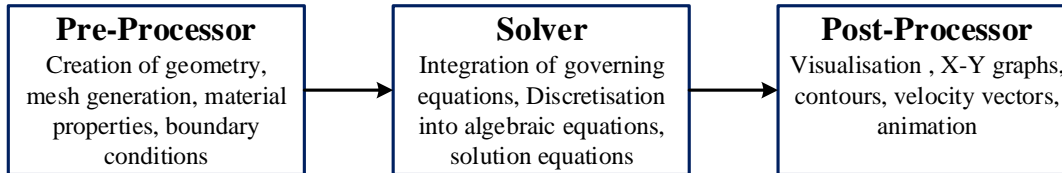


**Figure 3.1:** Flow chart for a typical CFD project [Versteeg and Malalasekera, 2007].

As seen in the flowchart, the pre-processor defines all the inputs needed for the problem. The first step for any CFD simulation is the definition and creation of the geometry. Secondly, a mesh is generated through a subdivision of the domain into a number of smaller cells. The number of cells and their internal coherence has a great influence on the computational time and accuracy of calculations. However, generally, a higher amount of cells also increases the accuracy of the solution. Therefore the crossover between accuracy and computational time is very important. The number of cells is usually determined based on grid independence study. Over 50% of the time spent in the industry on a CFD project is devoted to the definition of the geometry and generation of the mesh [Versteeg and Malalasekera, 2007].

The specification of appropriate boundary conditions, source-terms etc., is of great importance. The boundary conditions are used to initialize the solver, so realistic inputs are of great importance. Furthermore, the fluid properties are determined and set.

Following the pre-processor comes the solver. Here, the appropriate solver is chosen for the specific case. The governing equations are integrated over each of the cells in the constructed mesh. Afterwards, the integrated equations are discretised into a set of algebraic equations which are solved using an iterative method to obtain the final solution [Versteeg and Malalasekera, 2007]. The algebraic form of the equations governing the fluid flow are approximated by application of different finite difference approximations to the finite volume cell. For the faces at each cell, the surface fluxes are determined through different interpolation schemes [Tu et al., 2007].

Lastly, the solution data is loaded into the post-processor. Here the different data can be visualised with the help of different tools which helps create an overview of the results using, contours, vector and surfaces plots in both 2D and 3D. In the case of transient simulations, dynamic animations can be made, showing the fluid flow behaviour as a function of time.

Accurate numerical work is important for decreasing the cost of performing expensive experimental work and helps to give a deeper insight into the fluid dynamic behaviour of the system. In the following section 3.2, the geometry constructed for this thesis will be presented and the different considerations regarding simplification will be highlighted.

### 3.2 Geometrical considerations

The first thing to consider when doing a numerical CFD analysis is whatever the geometry of application can be simplified. Being able to simply the geometry means that fewer cells might be needed, however, it is important to not simplify the geometry so much that the accuracy of the solution drops. One of the simplest forms for geometry simplification is due to symmetry. If the geometry is symmetrical around some axis, the results predicted on one side should be the mirrored results of the other and vice-versa. At first the geometry of the fuel cell stack showed in figure 1.8 on page 16 does not seem symmetrical due to the shape of the aluminium clamps. However, the flow field inside manifold part is very symmetrical due to the shape of the manifold. The geometry is not only symmetrical about one axis, but about two as can be seen in figure 3.2.

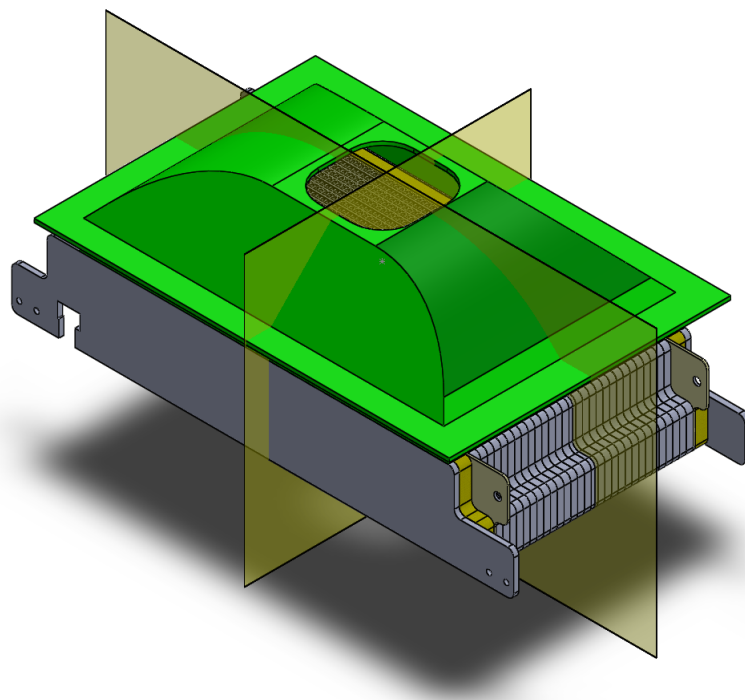


**Figure 3.2:** Figure showing the symmetrical lines of the manifold.

Even though the geometrical shape of the manifold is symmetrical, it does not necessarily mean that the geometry can be simplified. The reason for this is that the manifold is placed on top of the PEM fuel cell stack. In order to do the simplification it has to be placed symmetrically around the flow channels. This, however, is the case for the manifold of consideration.

The distance from the manifold to the first flow channel is  $1.6\text{mm}$  in both ends of the longest symmetry plane shown in figure 3.2 and the distance from the manifold wall to the cell is  $12\text{mm}$  for both sides of the smaller symmetry plane.

This means that only  $1/4$  of the stack needs to be meshed and numerically simulated. The results from these simulations can be mirrored to display the contours of the entire PEM fuel cell stack. For clarification, the  $1/4$  stack is shown in figure 3.3 where the distances mentioned above are indicated with a red circle for the  $1.6mm$  and blue circle for the  $12mm$ .

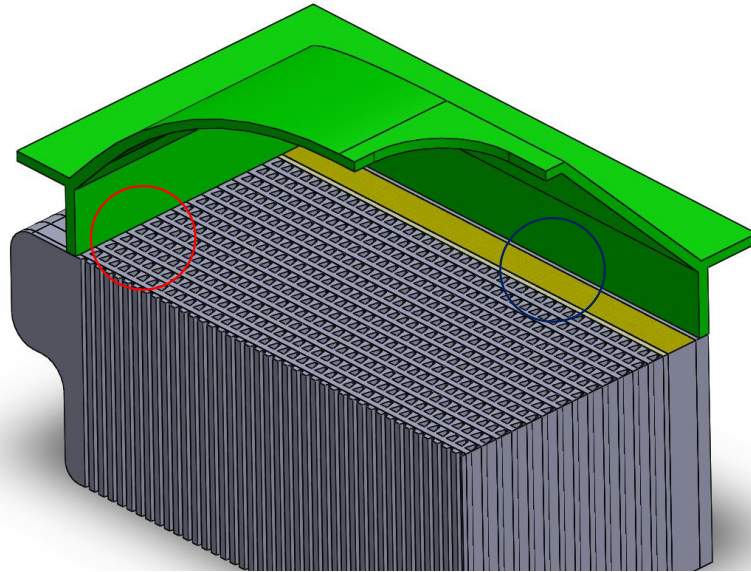


**Figure 3.3:** Figure highlighting the distances from the stack to the manifold.

As seen throughout the literature study, a porous media approach can be used to simplify the cells of the PEM fuel cell stack. Therefore the remaining parts of the cells covered by the manifold were all replaced by a single body (porous media). Since the geometry of interest is the flow inside the manifold, the remaining solid parts will be considered as walls and will not be a part of the geometry being meshed. The part of the geometry that is to be meshed can be seen in figure 3.4, the red body is the porous media (cells) remaining after the symmetry simplification of the main geometry. The blue part represents the volume of the open space inside the manifold where the air is flowing when the fan is running.

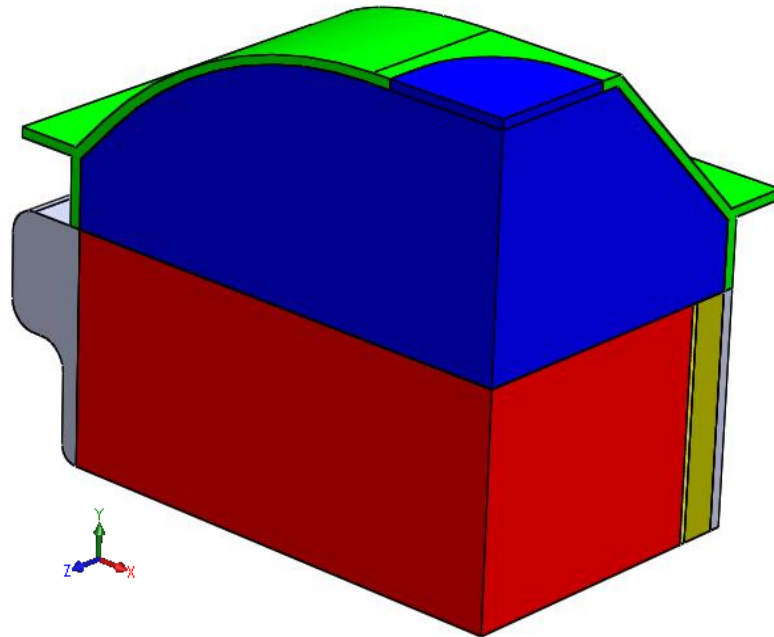


**Figure 3.4:** Figure showing the stack and manifold flow domain.

The fan is mounted on top of the manifold opening and will not be considered as a part of the geometry. Therefore the opening at the top of the manifold will be considered as the flow outlet for the simulations. The porous media will be extended with an inlet flow domain having the same size as the porous media in the x- and z-direction as seen in figure 3.4. However, it will be extruded in the y-direction and have two times of the length of the porous media. The air flow rate through the stack is due to suction from the fan at the top of the manifold.

The area before the inlet of the stack can be seen as a big reservoir filled with air. The flow that reaches the inlet side of the porous media (stack) is therefore not a fully developed flow and that is the reason for the very short inlet flow domain (two times the porous media depth).

### 3.3 Meshing methodology

The purpose of this section is to present the mesh constructed for the simplified geometry presented in the preceding section. The different meshing methodologies used for this thesis will be discussed and a final mesh approach will be suggested. The different mesh quality parameters will be presented and discussed for the constructed mesh. The grid generation presents an important consideration in terms of computing the numerical solution to the governing partial differential equations of the CFD case [Tu et al., 2007]. A well-constructed mesh increases the likelihood of attaining the solution. The generation of a good mesh is tedious, but of great importance. A straightforward way of constructing a mesh does not exist since it is totally depending on the case

of interest. However, the use of a *structured mesh* is considered as the best approach for stability [Tu et al., 2007]. This is the use of quadrilaterals for (2D) or hexahedral for (3D) cases.

Therefore the mesh for the geometry presented in the preceding text will be meshed using a structured meshing approach whenever possible. However, the geometry does not consist of only rectangular bodies which decrease the possibility of using a structured mesh. The geometry can be considered as 3 parts: an inlet domain (rectangular), a porous media domain (rectangular) and a manifold domain which has an irregular shape.

The geometry has been meshed using the meshing tool inside ANSYS Fluent 19.0 workbench. From the important geometry it is possible to see that it consist of two domains of hexahedrals and a manifold part of tetrahedrons.

The auto-generated mesh can be seen in figure 3.5

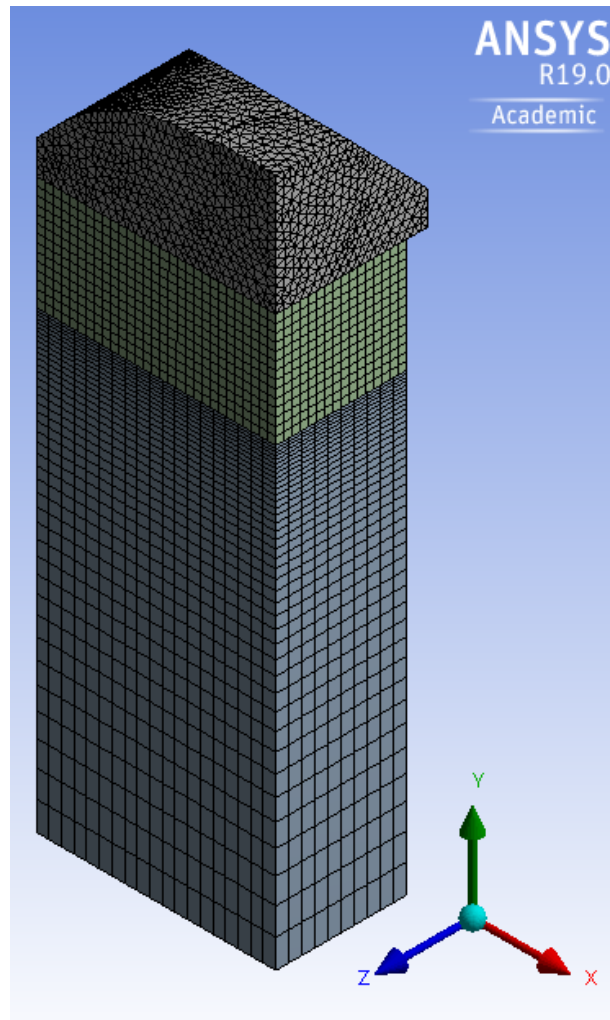


**Figure 3.5:** Figure showing the mesh of the geometry with the manifold part being highly unstructured.

### 3.3.1 Inlet domain

The purpose of the inlet domain is to act as the environmental surrounding from which the air is being drawn from. Due to the geometrical shape of the inlet domain, a purely structured mesh can be generated. The mesh is generated with the use of edge-sizing. The edge-sizing in the y-direction is specified with a certain number of divisions and a bias factor is used so that the mesh becomes more and more dense towards the inlet of the porous media. The edge-sizing in the x- and z-direction was specified with a certain element size, where the size was chosen to be two times the element size of that at the edge of the porous media. It means that one cell from the inlet domain would have the same width as two cells at the edge of the porous media. A figure showing the edge-sizing for the inlet flow domain can be seen in figure 3.6.

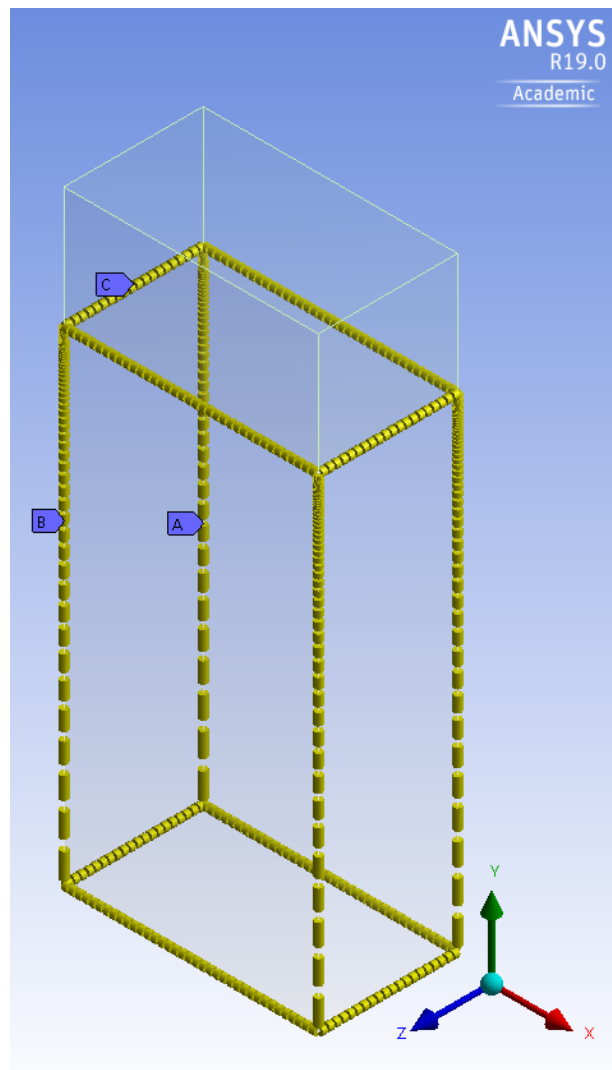


**Figure 3.6:** The edge-sizing used for meshing the inlet flow domain.

### 3.3.2 Porous media domain

The cathode channels of the PEM fuel cell is represented by a porous media with a specified loss-term which will be explained later throughout this thesis. The meshing of the porous zone is very simple. A constant body-sizing is used to specify the size of the elements within the zone. Due to the rectangular shape of the porous media, the mesh will be completely structured with hexahedral elements. The determination of the required element size will be determined by a grid independence study. The hexahedral mesh of the porous media domain can be seen in figure 3.7

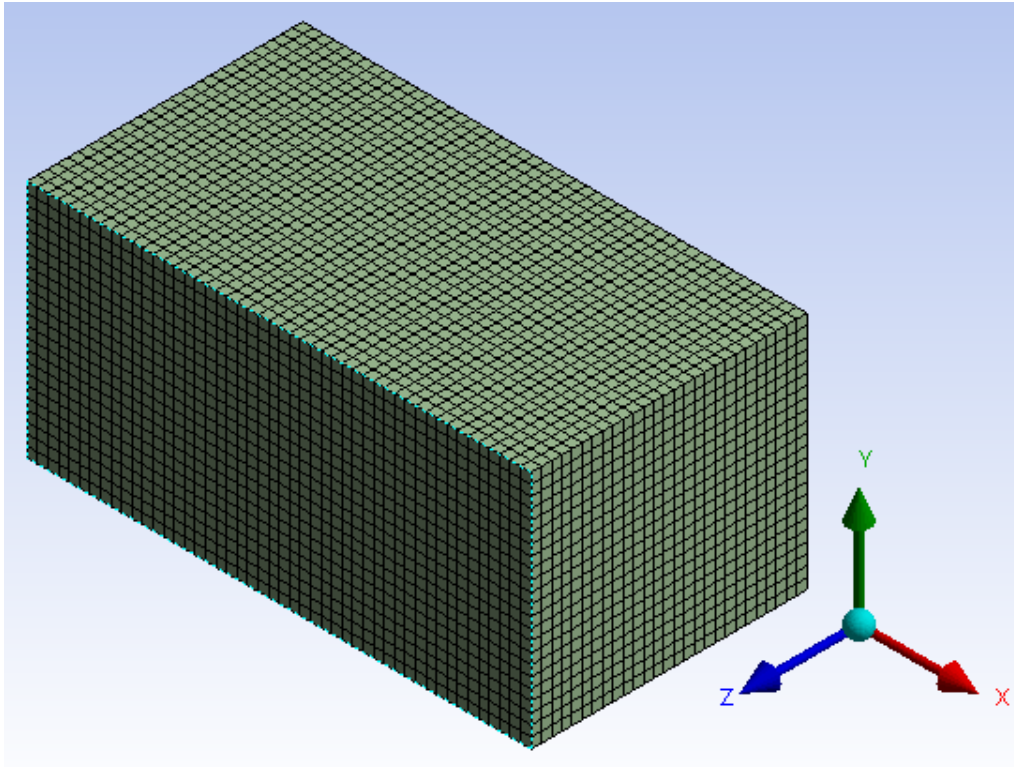


**Figure 3.7:** Figure showing the purely hexahedral mesh for the porous media.

### 3.3.3 Manifold flow domain

This subsection treats the modelling methodology applied for meshing the irregular flow domain inside the manifold. As seen in figure 3.5 on page 24, the manifold flow domain is an unstructured mesh of tetrahedrons. To make the mesh inside the manifold domain more structured, a decomposing of the current part was attempted. The purpose was to divide the part into smaller rectangular shapes which could be meshed with hexahedrals in a structured way.

In theory, it should be possible to decompose the flow domain into infinitesimal small rectangular shapes for a fully structured mesh. However, this process would be quite tedious and time-consuming. Therefore, the central parts of the flow domain were decomposed into rectangular shapes as can be seen in figure 3.8 on the next page.

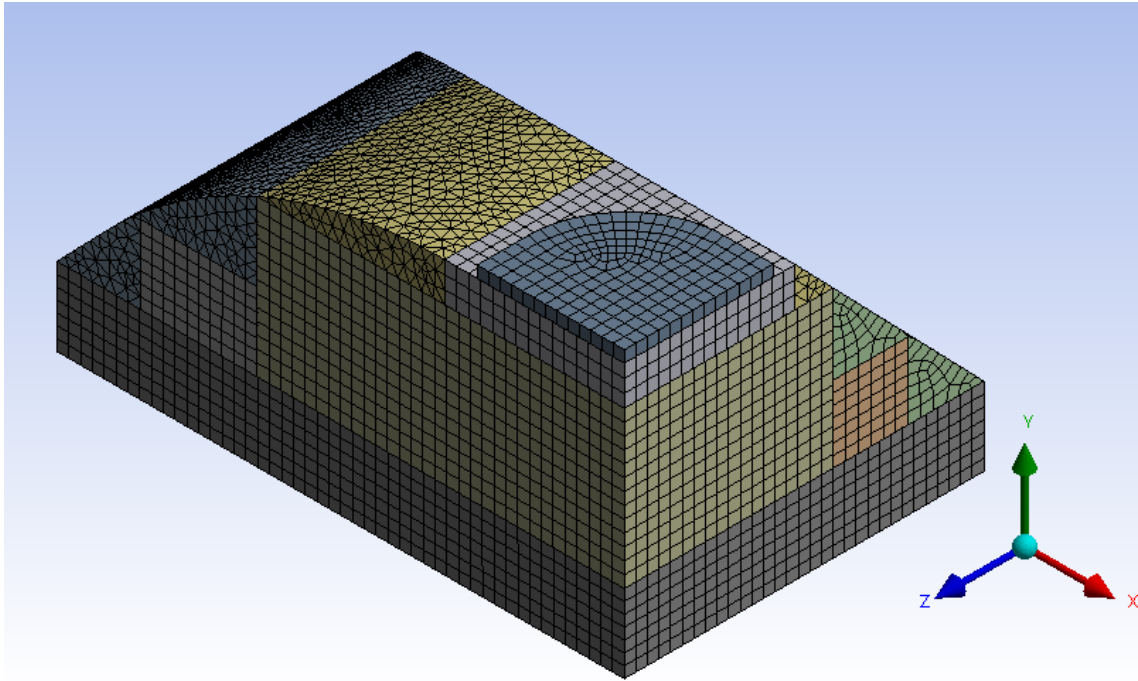


**Figure 3.8:** The decomposed manifold flow domain, a mixture of structured and unstructured cells.

In the decomposed manifold flow domain 82% of the cells are structured hexahedral cells while the remaining 18% is unstructured tetrahedrons. One of the disadvantages by the decomposing of the part is that a lot of interfaces is created between the different rectangles and irregular shapes. Even though Fluent should be able to handle the interfaces, and assign them correctly problems occurred and some of the interfaces had to be assigned correctly manually. As mentioned before this process was quite time-consuming and tedious, and changes in the geometry would require the process to be reworked. Therefore other methods were investigated to find easier and more straightforward ways of handling the geometry so that eventual geometrical changes could be handled without spending a lot of time decomposing the geometry.

After talks with the author of [Gao et al.], another meshing method was proposed for the irregular manifold domain. The author proposed to use the *MultiZone* method inside Fluent. The *MultiZone* method provides an automatic decomposition of geometry into mapped regions and free regions that are sweepable. When the *Multizone* method is used for meshing, all the regions selected are meshed with a pure hexahedral mesh if possible [ANSYS, 2018c].

For the regions where the model cannot be a mapped mesh the *hexa core* function allows the regions to be filled with a core of hexa cells. Hexa core can be generated where the majority of the volume is filled with a Cartesian array of hexahedrals elements where the tetrahedrons essentially are replaced. This core of hexahedral cells is connected to the remainder of a prism/tetra hybrid by an automatic creation of pyramids [ANSYS, 2018c]. The sweep edges function within the *MultiZone* method is used to select the edges that will influence the sweep path.

The usage of the MultiZone method allows changes in the original geometry to be re-meshed within an acceptable time frame. The quality of the mesh with the MultiZone method has been compared to that of the decomposed mesh and will be presented in the following mesh subsection. A cut-view of the manifold domain with the MultiZone method applied can be seen in figure 3.9

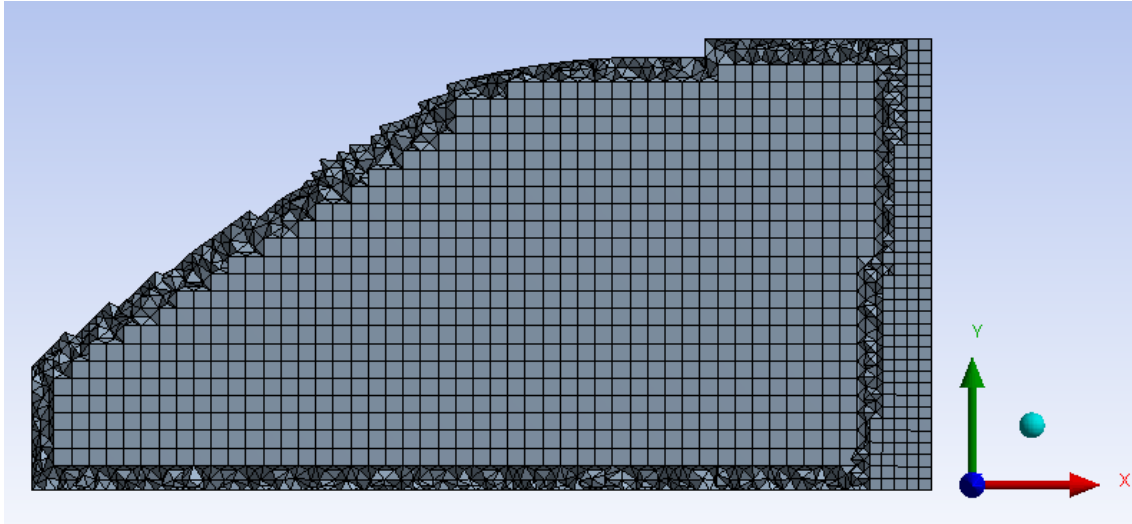


**Figure 3.9:** A cut-view showing the mesh inside the manifold domain.

### 3.3.4 Mesh quality parameters

This section is based on, [ANSYS, 2018c]. The mesh quality plays an important role in terms of solution accuracy, convergence and stability. Regardless of the type of mesh, it is important to note whether the quality of the mesh is sufficient.

#### Orthogonal quality

An important mesh quality parameter to monitor is the orthogonal quality, which Ansys meshing can display. For the determination of the orthogonal quality of each cell, the following equation can be used in calculating the orthogonal quality [ANSYS, 2014]:

$$\text{Orthogonal quality} = \min \left( \frac{\overline{A}_i \cdot \overline{f}_i}{|\overline{A}_i| |\overline{f}_i|}, \frac{\overline{A}_i \cdot \overline{c}_i}{|\overline{A}_i| |\overline{c}_i|} \right) \quad (3.2)$$

Where  $\overline{A}_i$  is the face normal vector,  $\overline{f}_i$  is a vector pointing from the cell center to the middle of the cell face and  $\overline{c}_i$  is the vector from the center of the cell to the center of a neighbouring cell, for which it shares a face. It is the minimum value calculated from all the faces that determines the orthogonal quality of the giving cell. This means that the best cells have a value of 1, while the worst cells have a value of 0.

### Aspect ratio

Another important mesh quality is the aspect ratio. The aspect ratio is a measure of stretching of the cell. It is difficult to determine what an ideal aspect ratio is, since this depends on how the gradients change from cell to cell. In cases where the gradients experience strong changes, the aspect ratio should be small.

### Cell skewness

The skewness is one of the primary quality measures for a mesh. The skewness determines how close to ideal an element or face is (equilateral or equiangular). Highly skewed cells can make the calculations unstable and decrease the accuracy of the solution. The maximum skewness can be calculated (in general) by the following equation [ANSYS, 2014].

$$\text{Skewness} = \max \left( \frac{\theta_{max} - \theta_e}{180 - \theta_e}, \frac{\theta_e - \theta_{min}}{\theta_e} \right) \quad (3.3)$$

Here  $\theta_{min}$  is the smallest angle, while  $\theta_{max}$  is the largest angle of the cell.  $\theta_e$  is the normalized angle,  $90^\circ$  for quadrilaterals and  $60^\circ$  for triangles.

According to the definition of skewness, a value of 1 corresponds to a highly skewed cell, while a skewness of 0 indicates an equilateral cell. Highly skewed cells are not desirable, and according to [ANSYS, 2018c] the measure of skewness can be categorised as in table 3.1.

**Table 3.1:** Table showing the range of skewness values and their corresponding cell quality in ANSYS [ANSYS, 2018c].

Excellent	Very Good	Fair	Poor	Bad
0-0.25	0.25-0.50	0.50-0.75	0.75-0.9	0.9-1

According to [ANSYS, 2018c], a quality mesh has a skewness value of approximately 0.4 for 3D. The table 3.1 above is a general guide to the relationship between the cell skewness and quality.

For cases involving a 3D mesh, the cells should be within the good category or better. However, a small percentage will generally be in the fair range and there are usually even a few poor cells [ANSYS, 2018c].

For the constructed mesh, these parameters are of great importance and very important to monitor. However, as the grid density is increased or decreased, the corresponding quality parameters might change.

A grid independence study will be presented in 3.8 on page 42 and after refining the mesh, the quality parameters mentioned above will be evaluated. It is important to note that those quality parameters are a measure of the grids quality, however, it is possible to get accurate solutions, even if the mesh is poor in some regions.

### 3.4 Material properties and boundary conditions

This section will round off the set-up of the pre-processor as shown in figure 3.2 on page 21. This section will highlight the determination of the material properties used for the simulations as well as covering the determination of boundary conditions, pressure loss coefficients and source terms.

The determination of proper material and boundary conditions are essential for representing real physical behaviour in terms of heat and mass transfer within the fluid domain. Also assigning boundary conditions carefully may help towards convergence due to the initial conditions present for the calculations [Tu et al., 2007].

#### Material properties

For the modelling of the PEM fuel cell stack, two properties have been used. Air is an essential part of the open cathode configuration for the PEM fuel cell. Not only does it supply the oxygen for the chemical reaction, but is also needed for the essential cooling of the stack to prevent it from overheating and prolonging its lifetime [Ballard, 2011]. Besides air, properties for the solid part of the fuel cell stack have been utilised. The stack consists mostly of graphite, therefore, the solid will be considered purely as graphite where the thermodynamic properties used are from [Gao et al.], these can be seen in table 3.2.

**Table 3.2:** Table showing the material properties used [Gao et al.].

Properties	$\rho$ [kg/m <sup>3</sup> ]	$C_p$ [J/kg·K]	$k$ [W/m·K]	$\mu$ [kg/m·s]
Air	1.225	1006.43	0.0242	1.7894e-05
Graphite	2250	1732	24	-

The thermodynamic properties of the materials have great influence for example on the temperature distribution inside the fuel cell stack and the temperature of the air leaving the stack.

### 3.4.1 Boundary conditions

This subsection will outline and explain the different boundary conditions for the flow domain. These include an inlet, an outlet and different wall boundary conditions. The different boundary conditions, that have been utilised, can be seen in figure 3.10.

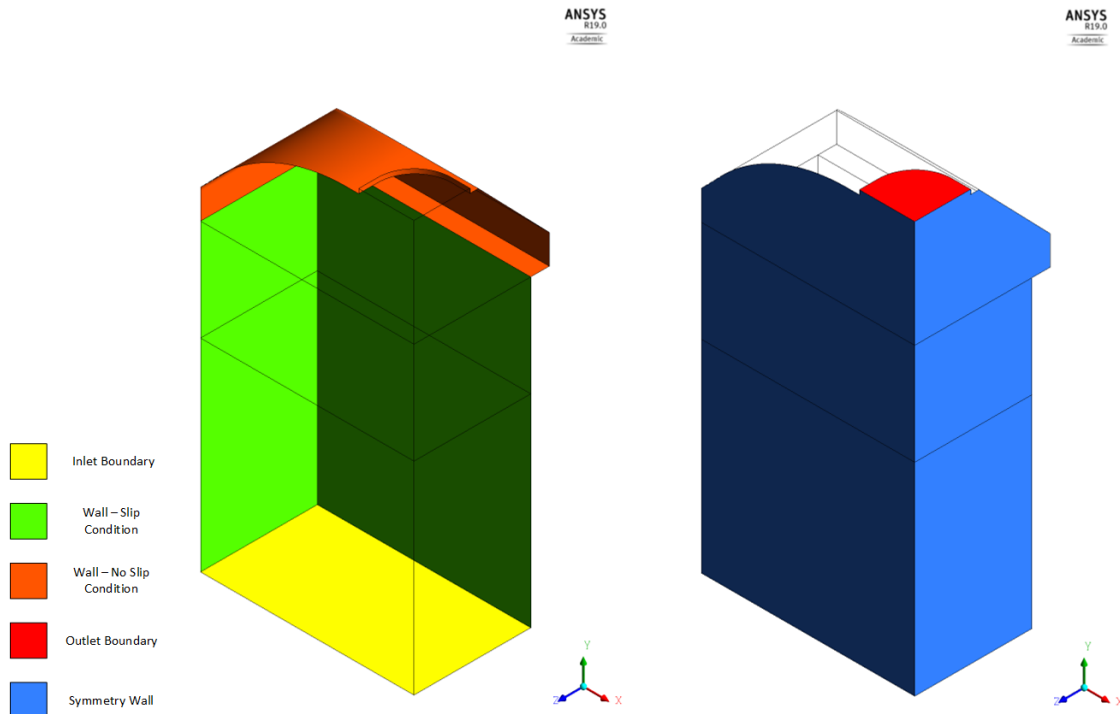


**Figure 3.10:** The figure shows the different applied boundary conditions for the numerical simulations.

#### Wall boundary

The walls represented by the orange color in figure 3.10 acts as walls with a no-slip boundary condition imposed. The no-slip conditions specifies that the velocity components are zero at the boundary wall, that is that  $u = v = w = 0$  [Versteeg and Malalasekera, 2007]. The flow in the model is assumed laminar, therefore the flow is independent of the pipe roughness, since the flow is stratified and covers the roughness.

The green color represents walls with a specified slip condition. The inlet flow domain can be considered as a tank from which air is being pulled when the fan at the manifold top is operating. This tank is, in reality, infinite large therefore there is no wall affecting the flow. As for the porous media, using a no-slip condition would basically mean that the entire stack is considered as one large duct which is not the case, however, should a no-slip condition be used all the cathode flow channels would have to be meshed, therefore a slip condition has been chosen.

### Symmetry boundary

As mentioned at the beginning of this chapter in section 3.2 on page 21, the geometry has been simplified. This means that only 1/4 of the stack is being simulated. However, to show the results for an entire stack, the results from the simulation are mirrored about the x-axis and afterwards around the z-axis or vice-versa. Applying symmetry wall conditions implies that the walls are considered as walls with a slip condition.

### Outlet boundary

The outlet of the flow domain is on top of the manifold, due to the fact that the fan is pulling air through the stack. The outlet boundary has been specified as an exhaust fan. The boundary conditions are basically the same as a pressure outlet, however, it allows for the specification of a pressure jump. For this numerical model, the exhaust fan acts as a pressure outlet, where the static (gauge) pressure at the boundary has been specified to 0 implying atmospheric pressure at the outlet [ANSYS, 2018b].

### Inlet boundary

For the inlet boundary, a velocity inlet condition has been chosen. Magnitude and direction are normal to the boundary. The stagnation pressure is not fixed, but will continue to rise in response to the computed static pressure until the value necessary to provide the desired velocity distribution has been reached.

To determine the dirichlet boundary condition at the inlet, an equation taking into account mass flow rate, density and area is needed. In general, the velocity can be described as:

$$v = \frac{\dot{m}}{A \cdot \rho} \quad (3.4)$$

Where  $A$  is the cross-sectional area of which the fluid is flowing through,  $\rho$  is the density of the fluid and  $\dot{m}$  is the mass flow rate. The only fluid used for the numerical simulations is air. The air needs to supply oxygen for the chemical reactions and to remove the excess heat released from the reactions. The density of air can be approximated using the ideal gas equation. Since the volume  $V$  is:

$$V = \frac{n \cdot R \cdot T}{P} \quad (3.5)$$

Where  $n$  is the number of moles and can be expressed as the mass  $m$ , divided by the molar mass  $M$ .

$$n = \frac{m}{M} \quad (3.6)$$

Substituting the expression for  $n$  in equation 3.6 into equation 3.5 and recalling that density is mass per volume. Dividing both sides by  $m$  and inverting the equation, yields an expression for the density as:

$$\rho = \frac{M_{air} \cdot P}{R \cdot T} \quad (3.7)$$

As mentioned in subsection 1.1.4 on page 7, the air flow rate at the cathode inlet has to be equal to or higher than the rate at which the reactants are consumed at the fuel cell. Based on Faraday's law an expression for the mass flow rate through the cell can be expressed as [Barbir, 2005]:

$$\dot{m}_{O_2} = \frac{I}{n_e \cdot F} \cdot M_{O_2} \quad (3.8)$$

Where,  $I$  is the current,  $n_e$  the number of electrons per mole of oxygen (4) and  $F$  is the Faraday's constant.

However, for fuel cells the current is often defined as a current *density*  $i = A/cm^2$ , which is the current per unit active electrode area [Ramani, 2006]. For the Mark1020 - PEM fuel cell the active electrode area is  $200cm^2$  [Berning, 2018]. Due to the addition of an area depending current, a corresponding area is needed for the units to match. Therefore the membrane electrode assembly (MEA) is introduced in the equation, the equation for the mass flow of air for a single channel can be described as:

$$\dot{m}_{air} = \frac{i}{4 \cdot F} \cdot A_{MEA} \cdot M_{air} \quad (3.9)$$

The MEA is simply the width of one PEM cell assembly, multiplied by the length of the assembly and can be seen in figure 3.11, where the area  $A$  in equation 3.4 also are depicted. The area  $A$  is represented by the red color and is the frontal area of the channel. The blue part represents the width and length of one cathode channel MEA.

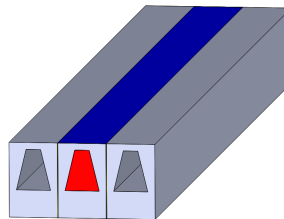


**Figure 3.11:** Figure showing the area  $A$  (red), and the MEA area (blue).

Adding the expression for the area  $A$ , into equation 3.4, together with the expression for density in equation 3.7 and the mass flow rate of oxygen 3.9 yields:

$$v = \frac{i}{4 \cdot F} \cdot A_{MEA} \cdot M_{air} \cdot \frac{R \cdot T}{M_{air} \cdot P} \cdot \frac{1}{A} \quad (3.10)$$

Since equation 3.9 is the required amount of oxygen needed for the reaction an correlation is introduced by the fact that air contains approximately 21% oxygen [Ballard, 2011]. However, stoichiometry is used to ensure that there are in fact the required amount of oxygen needed. Ballard specifies that the stoichiometry should not be less than 10 and preferably 50 or higher. Therefore this is introduced into equation 3.10, after simplifying the equation, a final expression for the velocity inlet at the cell can be expressed as:

$$v_{cell} = \frac{i}{4 \cdot F} \cdot \frac{1}{0.21} \cdot A_{MEA} \cdot \frac{R \cdot T_{air}}{P_{in}} \cdot \frac{1}{Area_{channel}} \cdot \zeta_{stoich} \quad (3.11)$$

Since this is the required velocity at the cathode channel inlet, the actual free-stream velocity will be less due to the porosity of the fuel cell stack. However, Fluent uses a superficial velocity approach for the velocity across the porous zone meaning that the velocity specified at the inlet boundary would be the superficial velocity in the porous region. Therefore, the inlet velocity calculated from equation 3.11 has to be multiplied by the porosity of the stack. The stack porosity  $\gamma$  has been evaluated from the constructed CAD drawings to be 0.27, the expression for the inlet boundary becomes:

$$v_{boundary} = v_{cell} \cdot \gamma \quad (3.12)$$

### 3.5 Energy equation considerations

Flow of thermal energy from matter in one region in space to matter occupying a different region in space is known as heat transfer. The occurrences of heat transfer can be separated into three main methods: convection, conduction and radiation. The physical models involving conduction and convection are the simplest [ANSYS, 2018a]. For the parts of the domain not containing the porous media, ANSYS Fluent solves the standard energy transport equation [ANSYS, 2018a]:

$$\frac{\partial}{\partial t}(\rho E) + \nabla \cdot (\vec{v}(\rho E + p)) = \nabla \cdot \left( k_{eff} \nabla T - \sum_j h_j \vec{J}_j + (\vec{\tau}_{eff} \vec{v}) \right) + S_h \quad (3.13)$$

Where  $E$  is the total energy,  $k_{eff}$  is the effective conductivity,  $\vec{J}_j$  is the diffusion flux of species  $j$ ,  $\vec{\tau}_{eff}$  is the shear stress tensor and  $S_h$  is an volumetric heat source. The three terms of the right hand side of the equation represent heat transfer due to conduction, species diffusion and

viscous dissipation, respectively [ANSYS, 2018a]. While the terms of the left hand side represent the transient and convective term, respectively.

However, for the porous region the standard energy transport equation is solved with modifications to the conduction flux and the transient terms only [ANSYS, 2018b]. There are two thermal models for the porous zone: an equilibrium model and a non-equilibrium model. For the equilibrium model, the porous medium and fluid flow are assumed to be in thermal equilibrium, the conduction flux within the porous medium uses an effective conductivity. While the transient term includes thermal inertia of the solid region in the porous media:

$$\frac{\partial}{\partial t} (\gamma \rho_f E_f + (1 - \gamma) \rho_s E_s) + \nabla \cdot (\vec{v}(\rho_f E_f + p)) = \nabla \cdot \left( k_{eff} \nabla T - \left( \sum_i h_i J_i \right) + (\bar{\tau} \vec{v}) \right) + S_f^h \quad (3.14)$$

Where  $\gamma$  represents the porosity of the porous region, the subscripts  $f$  and  $s$  indicates the fluid and solid respectively and  $S_f^h$  is the fluid source term. Where the effective thermal conductivity  $k_{eff}$  in the porous medium is represented by:

$$k_{eff} = \gamma k_f + (1 - \gamma) k_s \quad (3.15)$$

However, for the simulation of the PEM fuel cell stack the porous medium and fluid flow can not be assumed to be in thermal equilibrium. Therefore, a non-equilibrium thermal model is used, with this approach, a solid zone that is spatially coincident with the porous fluid zone is generated [ANSYS, 2018b]. The solid zone only interacts with the fluid in regards to heat transfer. Instead of solving one conservation equation for energy, the solid and fluid zones are solved respectively. Where the conservation equation for the fluid zone is [ANSYS, 2018b]:

$$\frac{\partial}{\partial t} (\gamma \rho_f E_f) + \nabla \cdot (\vec{v}(\rho_f E_f + p)) = \nabla \cdot \left( \gamma k_f \nabla T_f - \left( \sum_i h_i J_i \right) + (\bar{\tau} \vec{v}) \right) + S_f^h + h_{fs} A_{fs} (T_s - T_f) \quad (3.16)$$

Where  $h_{fs}$  is the heat transfer coefficient for the interface between the fluid and solid and  $A_{fs}$  is the interfacial area density, the ratio of the area of the interface of the fluid/solid and the volume of the porous medium. For the solid zone, the energy equation is [ANSYS, 2018b]:

$$\frac{\partial}{\partial t} ((1 - \gamma) \rho_s E_s) = \nabla \cdot ((1 - \gamma) k_s \nabla T_s) + S_s^h + h_{fs} A_{fs} (T_f - T_s) \quad (3.17)$$

To satisfy the above equations, both the heat transfer coefficient  $h_{fs}$ , interfacial area  $A_{fs}$  and the source term needs to be specified. The heat transfer coefficient has been estimated based on

previous work that used the same porous media approach, therefore the heat transfer is fixed as specified by [Gao et al.], to be  $40 \frac{W}{m^2 \cdot K}$ .

The interfacial area has been calculated based on the constructed CAD drawings of the Mark1020 PEM fuel cell stack. The interfacial area is basically the area of the channels where the flow *touches* the channel divided by the volume of the stack (porous media). The channel area that touches the flow, has been measured in Solidworks to be  $668.85mm^2$ , there is a total of 81 cooling channels per cooling plate and a total number of  $n+1$  plates exist where  $n$  is the number of cells (28), the volume of the porous media has been estimated to  $3.185 \cdot 10^{-3}m^3$ . This gives an interfacial density of:

$$Interfacial_{density} = \frac{1.571 \cdot m^2}{3.185 \cdot 10^{-3} \cdot m^3} = 493.2 \frac{1}{m} \quad (3.18)$$

For the source term, as mentioned in 1.1.5 on page 8, not all thermal energy can be converted into electrical energy, therefore heat is released. The amount of heat released could be approximated using equation:

$$Q_{heat} = (1.254V - V_{cell})In_{cell} \quad (3.19)$$

As could be seen in the polarization curve for the Mark1020 stack, the actual cell voltage  $V_{cell}$  in the above equation varies as a function of the current. The heat released from the stack, therefore, depends on the current drawn from the stack.

The unit for the source term is  $W/m^3$ , therefore the calculated  $Q_{heat}$  (which depends on  $V_{cell}$ ) is divided by the stack volume. A table summarising the different parameters specified for the energy equation can be seen in 3.3.

**Table 3.3:** Table summarising the parameters used for the energy equation.

Current A	Source Term $W/m^3$	Interfacial Density $1/m$	Heat Transfer Coefficient $W/m^2K$
10	35112.09		
20	83639.56		
30	137459.34		
40	192457.14	493.22	40
50	248527.47		
60	309573.63		
70	383507.69		

### 3.6 Momentum equation - considerations

For any flow, ANSYS Fluent solves conservation equations for mass and momentum. In the case where the flow is turbulent, additional transport equations are solved. The conservation of momentum in an inertial non-accelerating reference frame can be described by [Albring, 1967]:

$$\frac{\partial}{\partial t}(\rho\vec{v}) + \nabla \cdot (\rho\vec{v}\vec{v}) = -\nabla p + \nabla \cdot (\vec{\tau}) + \rho\vec{g} + \vec{F} \quad (3.20)$$

Where  $p$  is the static pressure,  $\rho\vec{g}$  and  $\vec{F}$  are the gravitational and external body forces. Other model dependent source terms are contained within  $\vec{F}$  [ANSYS, 2018a]. This equation is solved for the entire flow domain.

However, the porous media model incorporates an empirically determined flow resistance in the region of the flow domain defined as *porous* [ANSYS, 2018b]. Basically the porous media model adds a momentum source term to the standard fluid flow equation 3.20. The source term is composed of two parts a viscous loss term, and an inertial loss term and can be described as the first and second term in the Darcy equation. The added source term in ANSYS Fluent can be described as:

$$S_i = - \left( \sum_{j=1}^3 D_{ij} \mu v_j + \sum_{j=1}^3 C_{ij} \frac{1}{2} \rho |v| v_j \right) \quad (3.21)$$

Here  $S_i$  represents the source term for the  $i$ 'th ( $x$ ,  $y$  or  $z$ ) momentum equation,  $|v|$  represents the magnitude of the velocity and  $D$  and  $C$  are prescribed matrices [ANSYS, 2018b]. The momentum sink contributes to the pressure gradient within the porous media, effectively creating a pressure drop across the porous zone that is proportional to the velocity or velocity square within the zone [ANSYS, 2018b].

For the case of a simple homogeneous porous media the momentum source term, can be written as:

$$S_i = - \left( \frac{\mu}{\alpha} v_i + C_2 \frac{1}{2} \rho |v| v_i \right) \quad (3.22)$$

Where  $\alpha$  is the permeability and  $C_2$  is the inertial resistance factor.  $D$  and  $C$  is simply specified as diagonal matrices with  $1/\alpha$  and  $C_2$  respectively on the diagonals and zero for the other elements [ANSYS, 2018b].

The viscous and inertial resistance coefficients are defined the same way, a Cartesian coordinate system is used to define two direction vectors in 3D. The viscous and inertial resistance coefficients are then specified in each direction. For 3D simulations, the third direction is normal to the plane that is defined by the two specified direction vectors.

The resistance coefficients can be determined based on different approaches. However, for this project an empirical relationship for the pressure drop across the stack has been determined by [Ballard, 2011], based on experimental results as:

$$\Delta P = \frac{0.00592 \cdot (T_{stack} + 273)^{1.5}}{T_{stack} + 393} \cdot \frac{\dot{V}_{stack}}{(n + 1)} \quad (3.23)$$

Where  $\Delta P$  is the pressure drop in (Pa),  $T_{stack}$  is the tack temperature in degrees Celsius ( $^{\circ}C$ ),  $n$  is the number of cells for the stack (28) and  $\dot{V}_{stack}$  is the stack volume flow in (L/min).

The volumetric flow rate is very depending on the operating current of the stack. From equation 1.20 on page 8, the required mass flow rate for a given current could be calculated. However, this flow rate is the minimum required flow rate for the reactants, therefore, the stoichiometry is introduced to the equation and divided by the density to give the volumetric flow rate:

$$\dot{V}_{air} = \left( \frac{\frac{I}{n_e F} \cdot \frac{1}{0.21} \cdot M_{air} \cdot n \cdot \zeta_{stoich}}{\rho_{air}} \right) \quad (3.24)$$

To determine the pressure drop an expression for  $T_{stack}$  is necessary, [Ballard, 2011] specifies an empirical function for the optimal stack temperature as a function of current:

$$T_{opt} = 0.53 \cdot I + 26.01 \quad (3.25)$$

From equation 3.12 on page 34 the superficial velocity could be determined, meaning that it is possible to calculate the superficial velocity that corresponds to a given pressure drop. The optimal stack temperature, volumetric flow rate, superficial velocity and corresponding pressure drop across the stack can be seen in table 3.4 where a stoichiometric number of (60) has been used.

**Table 3.4:** Table showing the optimal temperature, volumetric flow rate, superficial velocity and corresponding pressure drop as a function of current.

Current	Optimal Temperature	Volumetric Flow Rate	Superficial Velocity	Pressure Drop
<i>A</i>	$^{\circ}C$	<i>L/min</i>	<i>m/s</i>	<i>Pa</i>
10	31.31	293.76	0.115	7.50
20	36.61	587.52	0.229	15.21
30	41.91	881.28	0.345	23.12
40	47.21	1175.04	0.459	31.22
50	52.51	1468.8	0.575	39.53
60	57.81	1762.56	0.689	48.02
70	63.11	2056.32	0.804	56.71

Based on the above calculations for the pressure drop and superficial velocity as a function of current, it is possible to create an XY plot for the pressure drop as a function of superficial velocity. From which it is possible to extrapolate to determine the coefficients for the porous media. A figure showing the XY-plot for the velocity and corresponding pressure drop can be seen in figure 3.12. From these data a quadratic curve function with an intersection in (0,0) has been determined which can also be seen in the figure.

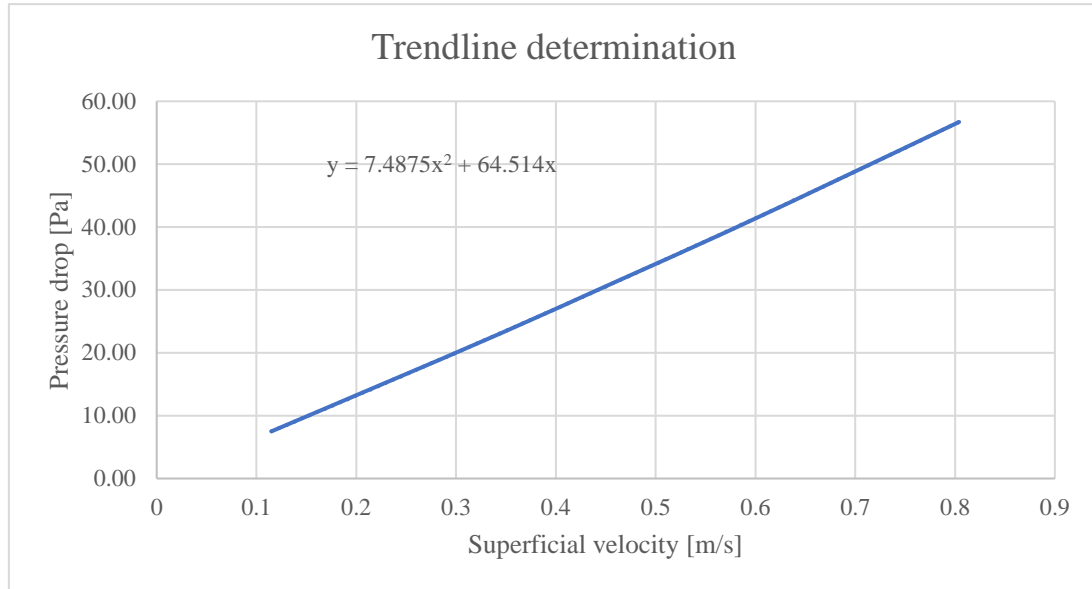


**Figure 3.12:** Figure showing the pressure drop across the stack, as a function of the corresponding superficial velocity.

This basically means that the pressure drop  $\Delta P$  can be related to the superficial velocity  $v_s$  as:

$$\Delta P = 64.514 \cdot v_s + 7.4875 \cdot v_s^2 \quad (3.26)$$

Where the two constants, must have the units of  $7.4875 = \text{kg}/\text{m}^3$  and  $64.514 = \text{kg}/\text{m}^2\text{s}$  for the units to add up.

A simplified version of the momentum equation, containing only the pressure drop and the source term can be written as:

$$\Delta P = -S_i \Delta n \quad (3.27)$$

Where  $\Delta n$  is the thickness of the porous media (70mm). Therefore, comparing equation 3.26 to equation 3.22 on page 37, yields expressions for the curve coefficients where the density  $\rho$

is assumed to be  $1.225\text{kg}/\text{m}^3$ , and the viscosity  $\mu$  is  $1.7894 \cdot 10^{-5}$ . The expressions for the curve coefficients can be seen in equation 3.28 and 3.29:

$$7.4875 = C_2 \frac{1}{2} \rho \Delta n \quad (3.28)$$

$$64.514 = \frac{\mu}{\alpha} \Delta n \quad (3.29)$$

ANSYS Fluent specifies that the prescribed matrices D and C in equation 3.21 on page 37, should specify  $1/\alpha$  and  $C_2$  on the diagonals. Therefore, solving the above equations yields the following coefficients for the viscous inertial resistance factor,  $\frac{1}{\alpha} = 5.15 \cdot 10^7$  and the inertial resistance factor,  $C_2 = 174.636$ . The units of  $\alpha$  in equation 3.29 are  $\alpha = \text{m}^2$ , and the units for  $C_2$  in equation 3.28 are  $C_2 = 1/\text{m}$ . This corresponds well to the ANSYS fluent setting where  $D = 1/\text{m}^2$  and  $C = 1/\text{m}$ .

This rounds off the pre-processor methodology used throughout this thesis. The geometry has been presented and simplified due to the symmetrical shape. A meshing methodology has been presented where two main methods have been explained and compared, that is the decomposed mesh and the MultiZone mesh. It was determined that the MultiZone mesh was the better due to convergence problems for the decomposed mesh. The MultiZone mesh had a great advantage compared to the decomposed mesh, due to the fact that it requires way less time to produce a good quality mesh in case of changes for the geometry and hence the flow domain. The material properties and boundary conditions have been presented, the considerations regarding the use of boundary conditions and determination of them have been highlighted. Furthermore, the changes in the energy and momentum equation for the porous media have been presented and explained. Different input parameters for the model have been explained and derived based on empirical formulas for the Mark1020 fuel cell stack.

### 3.7 Solution method

This section will outline the solution methods used for this project, as well as the different spatial discretization schemes used.

#### 3.7.1 Pressure-based solver

ANSYS Fluent allows the user to choose between one of two numerical methods: the pressure-based and the density-based. Historically the pressure-based solver was developed for low-speed incompressible flows, while the density-based solver mainly was used for high-speed compressible flows [ANSYS, 2018a]. The two solvers can be imagined to be an incompressible and a compressible solver. For this project, the pressure-based solver has been chosen, due to the fact that it is originally used for low-speed flows, however, both solvers have been upgraded and are applicable. At the same time a steady-state approach has been chosen, since the results of the solution do not change with time.

### 3.7.2 Pressure-based coupled algorithm

The pressure-based solver employs an algorithm that uses the projection method. For the projection method, the mass conservation (continuity) of the velocity field is achieved by solving a pressure correction equation. The pressure correction equation is derived from the continuity and momentum equations such that the velocity field, that is corrected by the pressure satisfies the continuity equation. The governing equations are non-linear and coupled, therefore the solution process involves iterations where all the governing equations are solved repeatedly until the solution is converged [ANSYS, 2018a].

Mainly two different algorithms exist for the pressure-based solver: the segregated algorithm and the coupled. As the name indicates the segregated algorithm solves the governing equations separately, while one equation is solved the others are *decoupled* the segregated algorithm is memory-efficient, but has slow convergence due to the fact that the governing equations are solved one at a time. Instead, the coupled algorithm can be used, here the equations comprising the momentum and pressure-based continuity equation are solved in a coupled system. Due to the fact that the momentum and continuity equations are solved in a coupled manner, the convergence rate of the solution is significantly increased. However, the required memory is increased due to the fact that the discrete system of both momentum and pressure-based continuity equations are stored [ANSYS, 2018a].

### 3.7.3 Spatial discretization schemes

The continuous equations have to be discretized. For this purpose different schemes can be used. This subsection will outline the once used for this project.

For the momentum equation the first order upwind scheme has been utilized, the scheme uses the one value upstream to evaluate the properties on the boundaries of the cell. A second-order upwind scheme can also be used, which is more accurate, since it utilizes two points upstream, however, due to the fact that it uses two points convergence is less stable for this project simulations with second-order upwind did not converge. For the energy equation, a second-order upwind scheme was used, the energy equation has less abrupt changes and converges with the higher order scheme.

For the pressure the PRESTO! pressure interpolation scheme has been chosen, however, for the porous media, a unique pressure interpolation scheme is used [ANSYS, 2018b].

The gradients are needed for constructing scalar values at the cell faces and for computing the velocity derivatives among other things. For this the least squares cell-based method has been used, here the solution is assumed to vary linearly. For irregular or skewed cells, the least-squares gradient method is comparable to that of the node-based gradient and both are superior compared to the cell-based gradient. However, the least-squares gradient is less expensive to compute compared to node-based gradient and is, therefore, the default gradient method in ANSYS Fluent [ANSYS, 2018a].

### 3.7.4 Under relaxation

For this project, the pseudo transient under relaxation has been used. Pseudo time-stepping is a technique used for solving steady-state solutions of time evolving partial differential equations by the use of an initial guess and using a time stepper to evolve the solution forward. The pseudo

transient time step is automatically calculated by ANSYS Fluent. However, the default explicit relaxation factors had to be lowered in order to achieve convergence.

### 3.7.5 Monitors

For the numerical calculations, the convergence criteria for the velocity and continuity equation residuals has been set at the default  $1 \cdot 10^{-3}$ . Likewise, the convergence criteria for the residual for the energy equation has been set at the default  $1 \cdot 10^{-6}$ . Besides residuals, the pressure drop across the porous media has been monitored to see, if the pressure has converged, likewise the maximum temperature of the flow domain has been monitored to see whether there are any changes with regards to the heat transfer.

To summarize the solution method section a table showing the different solvers, schemes etc. can be seen table 3.5.

**Table 3.5:** Table summarising the fluent set-up.

Fluent setting	
Convergence criteria	$1 \cdot 10^{-3}$ and $1 \cdot 10^{-6}$
Solver	Pressure based
Temporal state	Steady state
Solution algorithm	Coupled
Gradient evaluation	Least squares cell based
Pressure interpolation	PRESTO!
Momentum discretization	First order upwind
Energy discretization	Second order upwind
Under relaxation	Pseudo transient

## 3.8 Grid independence study

To ensure that the grid density is fine enough to resolve the solution, a grid independence study has been conducted. The grid density has gradually been increased from a very coarse mesh to a very fine mesh. The purpose of the study is to find a mesh density at which the solution does not change rapidly so that the solution variable can be considered to be converged. However, not only the solution accuracy is important, but also the computational time needed to obtain the solution is of concern.

For this grid independence study, an element size for the *porous media* and *manifold domain* has gradually been refined from an element size of  $5mm$  to an element size of  $1.5mm$ . While increasing the mesh density, the edge-sizing of the *inlet domain* has been scaled accordingly, so that one cell from the inlet domain has the same width as two cells in the porous media combined.

The main parameter that has been monitored is the pressure loss/drop across the stack (porous media). An empirical relationship for the pressure drop across the stack has been specified by [Ballard, 2011] and is presented later in this thesis under the determination of boundary conditions 3.4.1 on page 31. Therefore data for the actual pressure drop exists for both validation and comparison with the results from the grid independence study. Some of the main operating parameters used for the grid independence study can be seen in table 3.6 on the facing page.

**Table 3.6:** Operating conditions for the grid independence study

Ambient temperature	26.85°C
Stack current output	50A
Cathode stoichiometry	60
Superficial inlet velocity	0.689 $m/s$
Outlet gauge pressure	0 Pa

To determine the pressure drop across the porous media, a surface integral has been evaluated of both the inlet and outlet surface of the porous media. An area-weighted average of the total pressure has been evaluated for all surfaces. However, it should be emphasised that both the inlet and outlet respectively consist of two surfaces that are almost coincident, therefore, a small pressure drop exists between them.

The area-weighted average pressure drop, before the porous media is negligible due to the fact that the inlet domain act as a reservoir and not a duct. Therefore, the highest pressure evaluated at the inlet surface must be that of the inlet of the porous media. The highest pressure difference between the two coincident surfaces at the inlet has been determined to be  $1.35Pa$ , where the corresponding percentage difference between them is approximately 2.1%. The difference between the two surfaces drops as a function of mesh density.

As for the inlet, two almost coincident surfaces exist at the outlet of the porous media. Where the pressure difference between the two surfaces is almost exactly the same as for the inlet surfaces. However, the total pressure at the outlet is smaller than at the inlet, therefore, the percentage difference is larger, where the largest has been determined to be 4.3%. The outlet surface of the porous media, has been determined to be that with the highest total pressure of the two surfaces. This is due to the fact that additional pressure drop is observed over the manifold.

The pressure drop between the two surfaces, that has been determined to be the inlet and outlet of the porous media, has been plotted as a function of the mesh density. This can be seen in figure 3.13.

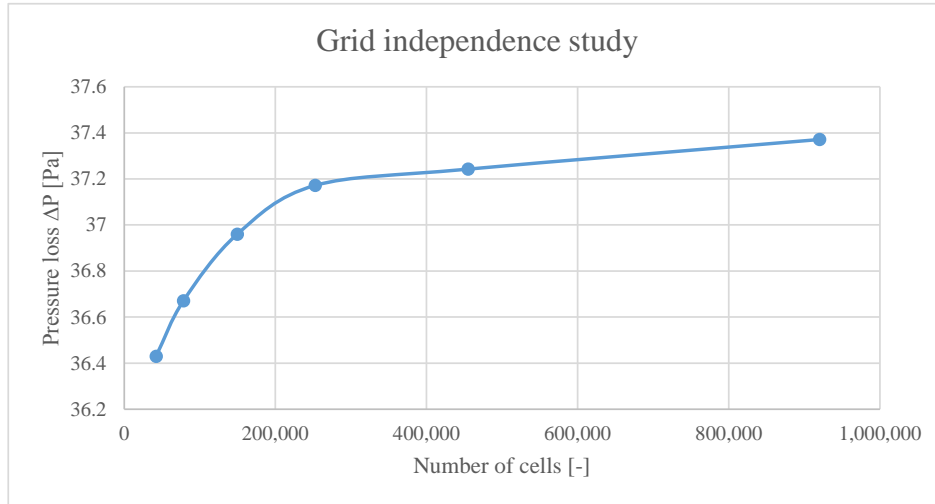


**Figure 3.13:** Figure showing the pressure loss across the porous media, as a function of grid density.

The figure shows that the solution for the pressure loss starts to converge at around 430,000 cells which correspond to a mesh grid size of 2mm. At the beginning as the mesh density is increased, the pressure loss over the porous media increases and starts to become flatter at around 200,000 cells. However, due to limitations on the available number of cells, simulations above 500,000 cells are prohibited. Therefore a mesh density of 2mm has been chosen for further simulations. During the grid independence study, the convergence criteria for continuity and velocity residuals were  $1 \cdot 10^{-3}$  while the convergence criteria for the energy residual were  $1 \cdot 10^{-6}$ . The number of iterations used for convergence, the time per iteration and the total time used for the simulations can be seen in table 3.7. The simulations were done using a workstation at the university with an Intel CPU Xeon E5-2687W v3 processor.

**Table 3.7:** Table showing the computational time required for each simulations, depending on the mesh density.

Mesh density	Time per iteration	Iterations for convergence	Total time
2 mm	0.9 seconds	280 iterations	252 seconds
2.25 mm	0.472 seconds	293 iterations	139 seconds
3 mm	0.272 seconds	252 iterations	96 seconds
4 mm	0.125 seconds	Not converged	-
5 mm	0.063 seconds	941 iterations	60 seconds

The general tendencies from the grid independence study are that the less refined mesh has a tendency to underpredict the results compared to a more dense mesh. This can be seen by introducing a *line* inside the flow domain and monitoring different parameters along that line.

Plotting the total pressure along such line shows that the less dense mesh does underpredict the total pressure compared to the more dense mesh. The total pressure along the line can be seen in figure 3.14.

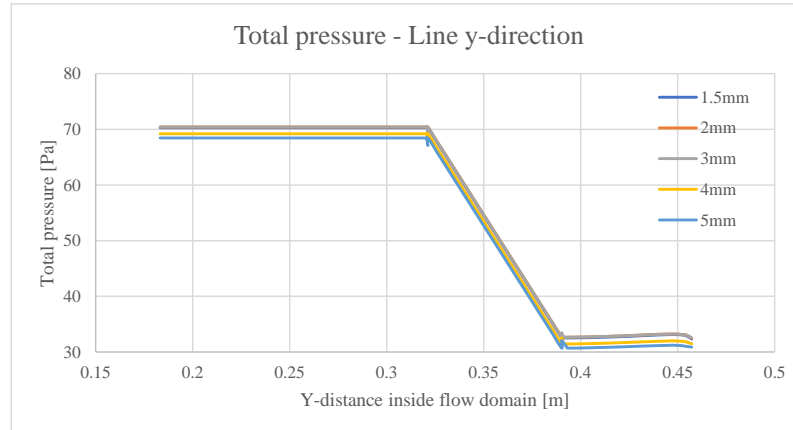


**Figure 3.14:** Figure showing the pressure loss along the y-direction.

As mentioned, due to limitations regarding the allowed number of cells a grid density of  $2mm$  has been chosen. The quality parameters mentioned in 3.3.4 on page 28 will be compared for the MultiZone and decomposed mesh. The values can be seen in table 3.8 and 3.9.

**Table 3.8:** Mesh quality of the domain using the MultiZone approach

MultiZone	Minimum	Mean	Max
Aspect ratio	1	1.9555	9.8595
Skewness	1.3057e-010	0.20028	0.80669
Orthogonal quality	0.19331	0.79468	1

**Table 3.9:** Mesh quality of the domain using the decomposed approach

Decomposed	Minimum	Mean	Max
Aspect ratio	1	1.4986	8.0213
Skewness	1.3057e-010	6.5396e-002	0.8595
Orthogonal quality	0.1405	0.93761	1

Both meshes contain fairly small aspect ratios. This is due to the body-sizing method used for both types of mesh. The regions containing higher aspect ratios are in the region just before the

porous media inlet, however, the stretching is in the x- and z-direction, where the gradients do not change rapidly, since the flow, is in the y-direction mostly.

The average skewness for both meshes are fairly low, especially the decomposed mesh has a small average skewness. This is due to the many rectangular shapes that the manifold has been decomposed into. For the MultiZone mesh, the cells containing a higher skewness are located in the outer region of the manifold where the cells are tetrahedrons. As mentioned in table 3.1 on page 29, cells with a skewness between 0.75-0.9 are of poor quality. The total number of cells with a skewness within this region for the MultiZone mesh is no more than 1400 cells.

As for the orthogonal quality, both meshes have a high average, however, the decomposed mesh seems to prevail in comparison to the MultiZone mesh. Therefore, based on the mesh quality parameters both meshes are of sufficient quality. However, the for the decomposed mesh simulations did not converge, this may be due to the many interfaces created as a consequence of the many different bodies. It was not possible to fix the problems regarding convergence for the decomposed mesh although the quality parameters, in general, were better than for the MultiZone mesh.

In order to validate the results of the numerical model constructed in this thesis, a parametric study of the pressure drop across the porous media as a function of superficial velocity has been conducted. The purpose of the parametric study is to vary the superficial inlet velocity to get a function for the pressure drop across the stack as a function of the superficial velocity. This function can be compared with the pressure drop from the empirical formula determined by [Ballard, 2011] based on experimental results. The superficial inlet velocity has been determined based on the current for currents ranging (10, 20, 30, 40, 50, 60 and 70) amps. Comparison between the numerical and empirical/experimental determined pressure drop across the porous media (fuel cell stack)

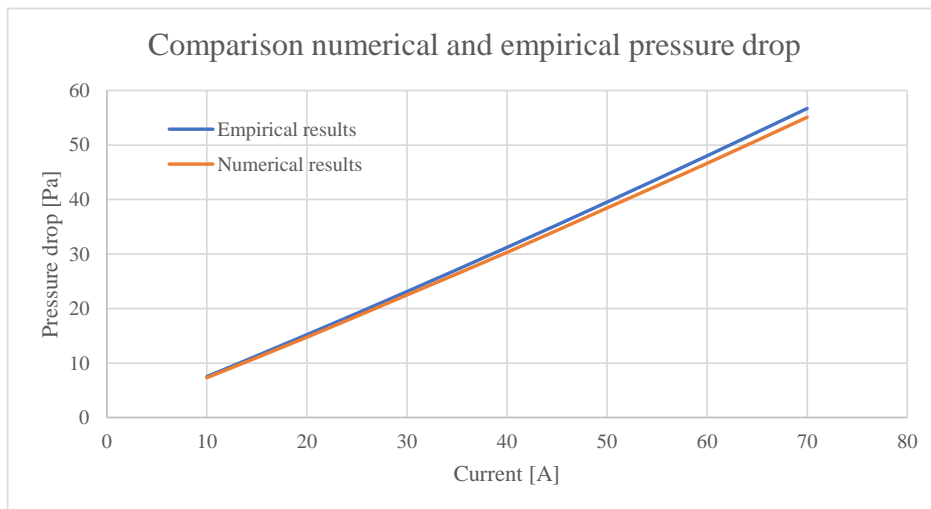


**Figure 4.1:** Figure showing the pressure loss for the empirical and numerical calculations.

The results show a good coherence between the numerical and experimental results. The biggest percentage wise difference between the numerical and experimental results are 3.16%, while the average difference is 2.87%. However, the general tendency is that the numerical results underpredict the actual experimental results. This may be due to the mesh density not being fine enough for the solution to be fully converged. As shown in the grid independence study the pressure drop for the numerical solutions was still increasing, with increasing number of cells.

## 4.1 Energy and mass balance

The conservation of mass and energy are essential for any model. The law of conservation of mass states that mass can neither be created nor destroyed. The net mass transfer to or from the system can be expressed simply as the difference between the inlet and outlet of the system. As for the comparison between the empirical and numerical pressure drop across the porous zone, the mass conservation has been investigated for the same cases. This means that it is the stack current that sets the inlet flow velocity and hence determines the inlet mass flow rate. A table showing the conservation between the inlet and outlet of the fuel cell stack for the different currents can be seen in table 4.1. The mass flow rates have been rounded up in the table, however, the original number has been used for calculating the percentage difference between the inlet and outlet with respect to the inlet.

**Table 4.1:** Table showing the mass conservation for the numerical model.

<b>Current (A)</b>	<b>Inlet flow rate <math>kg/s</math></b>	<b>Outlet flow rate <math>kg/s</math></b>	<b>Difference in flow rate <math>kg/s</math></b>
10	1.63E-03	1.63E-03	-1.01E-03
20	3.24E-03	3.24E-03	-1.54E-05
30	4.88E-03	4.88E-03	-4.31E-05
40	6.49E-03	6.49E-03	1.65E-04
50	8.13E-03	8.13E-03	-4.06E-05
60	9.74E-03	9.74E-03	-5.32E-04
70	1.14E-02	1.14E-02	-9.68E-04

As can be seen in table 4.1, the difference between the inlet and outlet flow rate are negligible, therefore, the mass is conserved for the numerical models for all currents.

The conservation of energy principle, also known as the first law of thermodynamics, states that energy can neither be created nor destroyed during a process. To investigate the conservation of energy for the numerical models, the difference between the inlet and outlet energy transfer rate for all the previously mentioned currents has been checked. As mentioned in section 3.5 on page 34, the heat released within the fuel cell stack depends on the operating current. The higher the current, the larger the amount of heat released. As mentioned in section 3.5 on page 34, a heat source term is implemented within the numerical model to simulate the heat released due to the chemical reaction within the stack. The heat source term has the units  $W/m^3$  and is implemented for the solid part of the porous media. Investigation of the difference between the inlet and outlet energy transfer rate should yield the contribution from the source term. The contribution from the source term, as a function of different currents (hence different source terms), can be seen in table 4.2.

**Table 4.2:** Table showing the difference between the inlet and outlet energy transfer rate.

<b>Current</b>	Inlet energy transfer rate	Outlet energy transfer rate	Difference in energy transfer rate
<i>A</i>	<i>W</i>	<i>W</i>	<i>W</i>
10	3.027	30.974	27.947
20	6.028	72.634	66.606
30	9.082	118.507	109.425
40	12.083	165.284	153.202
50	15.136	212.968	197.832
60	18.137	264.619	246.482
70	21.165	326.527	305.363

Since the heat released is within the solid part of the porous media, dividing the difference between the inlet and outlet as calculated in table 4.2 with the solid volume should yield the source term, if energy is to be conserved. The volume of the porous media is  $7.964 \cdot 10^{-4} m^3$ , dividing the values calculated in the above table with the volume yields the *calculated source terms* as in table 4.3, where the original determined source terms are presented for comparison. The percentage difference between the calculated and the original source terms with respect to the original source term, are presented in table 4.3.

**Table 4.3:** Table showing the difference between the original source term, and those calculated based on the heat transfer rate in the numerical model

<b>Current</b>	Original source term	Calculated source term	Percentage difference
<i>A</i>	<i>W/m<sup>3</sup></i>	<i>W/m<sup>3</sup></i>	<i>%</i>
10	35112.09	35093.66	0.053
20	83639.56	83638.10	0.002
30	137459.3	137406.36	0.039
40	192457.1	192377.20	0.042
50	248527.5	248420.38	0.043
60	309573.6	309510.80	0.020
70	383507.7	383447.82	0.016

As can be seen in table 4.3, the percentage difference between the original source term and the one determined from the fluent calculations is no more than 0.053% at worst. Therefore, the conservation of energy holds for all simulations performed.



The purpose of this chapter is to highlight some of the results acquired from the numerical model, representing the Mark1020 PEM fuel cell stack. A substantial amount of information is available from the numerical simulations. This chapter will, therefore, highlight some of the most important numerical results obtained.

Before presenting the results, the author would like to inform the reader that mistakes regarding air density has been made. Doing simulations, a constant air density has been used. However, the temperature change of the air is of such order that the density changes by approximately 8%. This will increase the velocity through the porous zone, and hence alter the pressure drop and temperature. For a base case of 60A the pressure drop increases by approximately 5%. However, the uniformity between different sections of the flow in an XZ-plane is the only the magnitudes are different.

### 5.1 Numerical results

One of the key results from the simulations is the flow distribution through the fuel cell stack. As mentioned throughout this thesis, uniformity of the air flow is of utmost importance since a uniform flow ensures optimal operating conditions for the fuel cell stack [Barbir, 2005]. The numerical results showed great uniformity of the flow through the porous zone. The difference between the highest and lowest velocity through the cell is no more than maximum 6%. The simulation showed that the velocity through the stack is the highest at the center and decreases out towards the edge of the stack. A contour plot, showing the velocity magnitude of the stack, can be seen in figure 5.1. The representation is of half a stack, the results should be mirrored around the z-axis to obtain the velocity field for the entire stack. The numerical results show that the velocity is the highest at the center just above the fan and decreases outwards in a circular pattern.

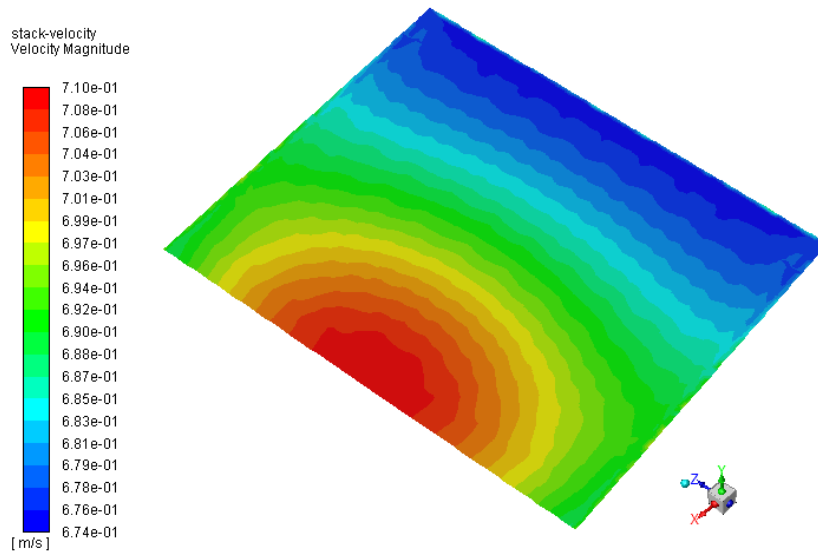


**Figure 5.1:** Contour plot showing the velocity magnitude of the air through the porous media at 60A operating conditions.

However, it should be emphasised that the fan outlet is represented as a pressure outlet. This means that there is no blockage of the flow through the outlet surface. As for the real case, the fan is located on top of the manifold creating a suction that pulls the air through the stack, but the fan has a hub part that significantly limits the flow in the center part of the outlet. This may have great influence on the flow uniformity of the stack.

Air is flowing through the cathode of the fuel cell stack to supply oxygen for the chemical reaction and to remove excess heat produced by the reaction. As a consequence of that, the air is heated as it flows through the fuel cell stack. A contour plot showing the increase in air temperature along the length of the channel (stack) can be seen in figure 5.2.

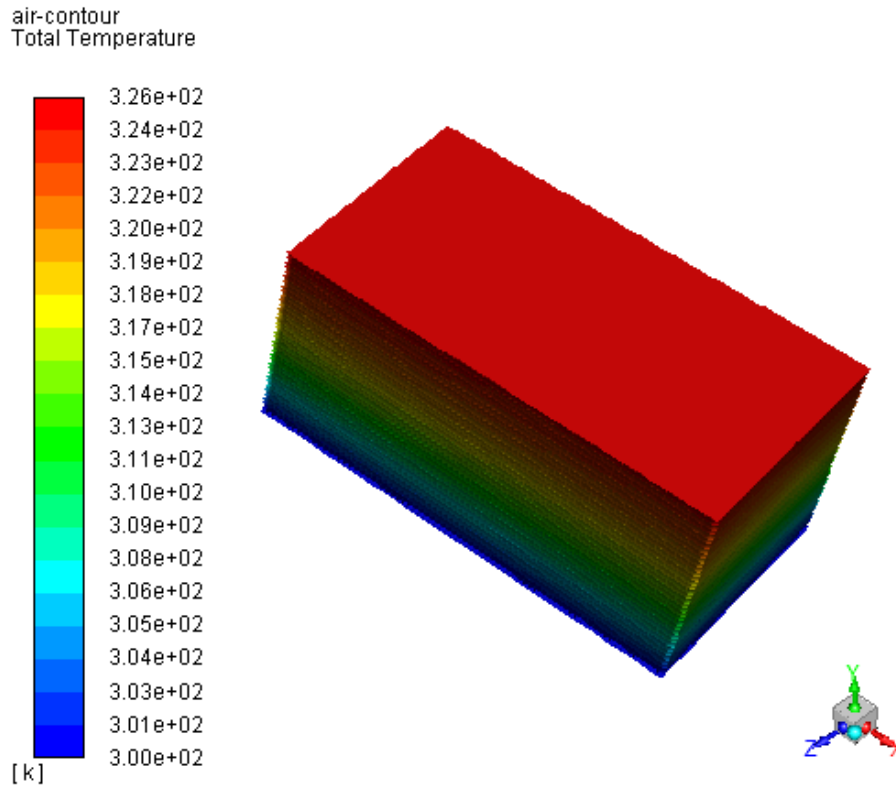


**Figure 5.2:** Contour plot showing the temperature of the air inside the porous media, at 60A operating conditions.

As can be seen in figure 5.2, the temperature in the xz-direction is highly uniform and increases in the y-direction, the direction at which the air is flowing. The highly uniform temperature distribution in the xz-plane is due to the velocity through the stack being uniform. Meaning that the time it takes for the air to go through each (channel) is approximately the same. Therefore, it experiences the same amount of heat from the solid part of the porous media.

The figure is a representation of  $1/4$  of the entire stack, however, mirroring the results would yield the same temperature distribution for the remaining part of the air flowing through the stack.

For the solid part, representing the bipolar plates, gas diffusion layers and so on, an assumption regarding the thermal conductivity has been made. As mentioned in the paper by [Gao et al.], the thermal conductivity of pure graphite is  $24 \text{ W/m}\cdot\text{K}$  which is the constant value used in this project. However, this may be significantly lower, due to the materials used. Also, the distribution of the thermal conductivity constant is placed along the diagonal of the  $3 \times 3$  matrix, meaning that the thermal conductivity is the same in the XX, YY and ZZ direction. However, due to different materials and especially the geometry of the actual stack, a more anisotropic approach would be more realistic.

The temperature distribution through the solid part of the stack has been visualised with a contour

plot and can be seen in figure 5.3.

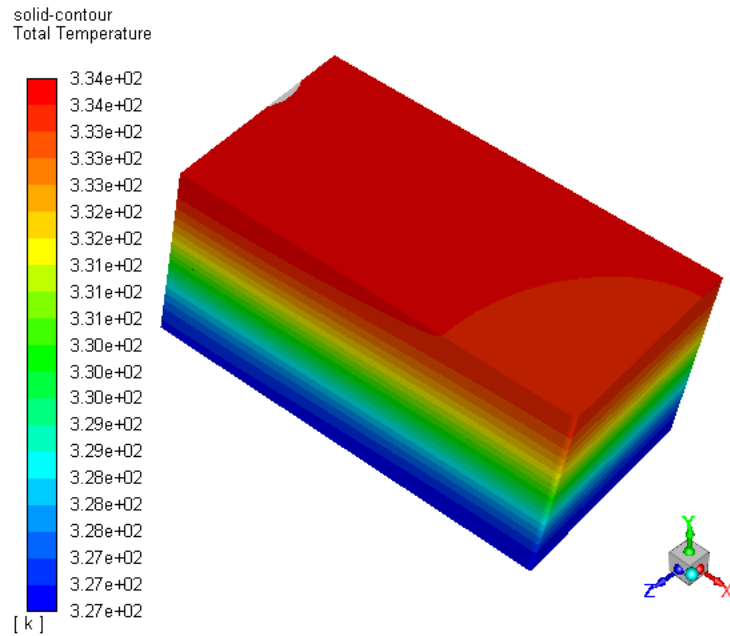


**Figure 5.3:** Contour plot showing the temperature distribution inside the solid part of the fuel cell stack, at 60A operating conditions.

The figure shows the same tendency as for the temperature of the air, however, the temperature is higher than that of the air, due to the use of the non-equilibrium thermal model. The temperature increases in the y-direction of the stack but is practically constant in the xz-plane. This is entirely due to the fact that the flow through the porous media is highly uniform, plotting the contour plot of the solid at the outlet would reveal a contour plot almost identical to that of the velocity as shown in figure 5.1.

As for the flow distribution inside the manifold, as the flow leave the porous stack it seeks towards the opening at the top of the manifold accelerating in velocity due to the area contracting at the manifold outlet. Plotting the velocity vectors for the flow inside the manifold shows that the distribution is neatly uniform. The velocity magnitude vectors inside the manifold can be seen in figure 5.4 on the next page.

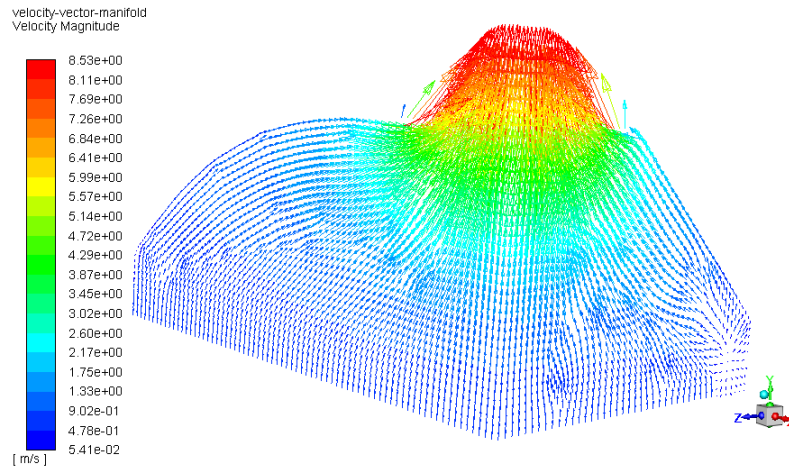


**Figure 5.4:** Figure showing the velocity magnitude, using vectors for the symmetrical manifold area.

However, at the bottom right corner, a small dispersion of the velocity vectors are seen. The corner represents an empty space between the porous media (fuel cell stack) and an aluminium panel where the manifold is mounted upon. It is possible to investigate the zone, by the use of pathlines. The pathlines for the symmetry plane of the manifold area can be seen in figure 5.5

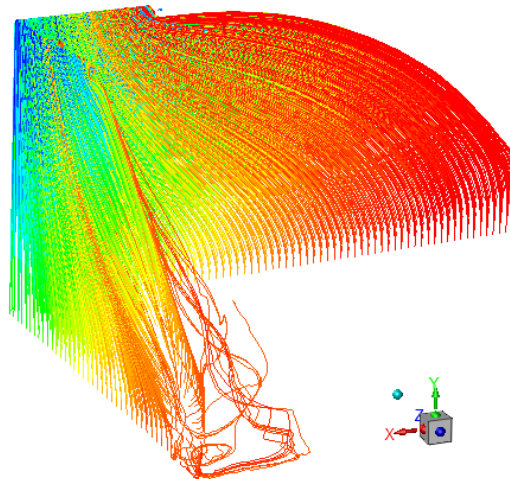


**Figure 5.5:** Contour plot showing the pathlines for the symmetrical manifold area.

Vorticity can be seen in the corner of the manifold where the vector dispersion evolved from. This is due to the fact that a small air *pocket* exist, creating a recirculation zone for the air. This vorticity has to break up before the flow is able to leave the manifold at the top.

Uniformity in the flow is a key parameter for obtaining optimal operating conditions for the fuel cell stack. The numerical results presented in figure 5.1, shows great uniformity for the flow through the stack with only a minor difference between the center of the stack and the top. Due to the highly uniform flow rate, a very even temperature distribution in the xz-plane was observed with temperature increasing in the y-direction only as the air temperature increases.

The optimal stack temperature for the Mark1020, stack can be represented in a more refined way using an empirical function from [Ballard, 2009]:

$$T_{opt} = 52.204 \cdot (1 - e^{-0.010 \cdot I}) + 38.095 \quad (5.1)$$

Where,  $T_{opt}$  is the optimal operating temperature in °C, and I is the current in Amps.

A paper by [Andisheh-Tadbir et al., 2014], specifies the location of the thermistor for the Mark1020 PEM fuel cell from Ballard. They state that the thermistor is located at about 0.88 of the channel length, measured from the cathode inlet. It is therefore interesting to monitor the cell temperature at that distance and compare the numerical results with that from [Ballard, 2009]. A figure showing the optimal temperature from the [Ballard, 2009] manual, and the corresponding evaluated stack temperature from the numerical model can be seen in figure 5.6.

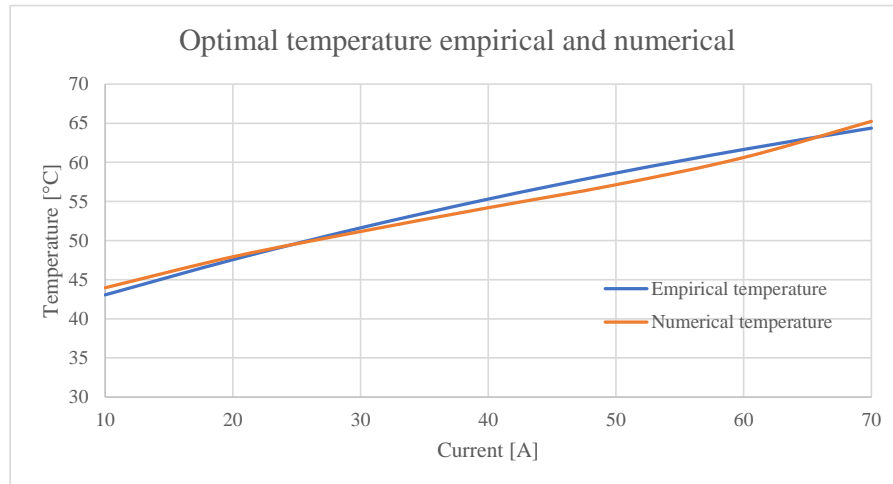


**Figure 5.6:** Figure showing the optimal temperature calculated from [Ballard, 2009], and the corresponding numerical results.

The figure shows great coherence between the empirical determined optimal temperature and the stack temperature 88% down the channel length. The maximum difference between the empirical results and the numerical results are 3%. However, it is important to notice that the stack temperature is a function of many variables, e.g. thermal conductivity, heat transfer coefficient and fluid velocity.

The numerical results presented in section 5 on page 51, showed great uniformity for the flow distribution. As a consequence of uniformity in the flow, an almost constant temperature profile in the XZ-plane was observed. As stated by [Andisheh-Tadbir et al., 2014], the thermistor for the Mark1020 stack is located 88% up the length of the cathode channel. The numerically determined temperature at this location corresponded well to the optimal temperature specified by [Ballard, 2009], as can be seen in figure 5.6 on the preceding page. However, the Mark1020 stack used for Team Aalborg Energy's car Cimbrer II is located in the *trunk* of the car. While the car is driving, the trunk is sealed with an *engine hood* which limits the amount of fresh air entering the *trunk* of the car. As a consequence, most of the air inside the *trunk* is recycled through the PEM stack. As shown in figure 5.2 on page 53, the air flowing through the stack is heated due to heat transfer with the solid part of the stack. This means that with time, warmer and warmer air will be utilised at the cathode inlet increasing the overall stack temperature. Since the *trunk* of the car has an approximated volume of  $\approx 700L$ , increasing air temperature cannot be neglected. The placement of the Mark1020 stack, inside the *trunk* can be seen in figure 6.1.

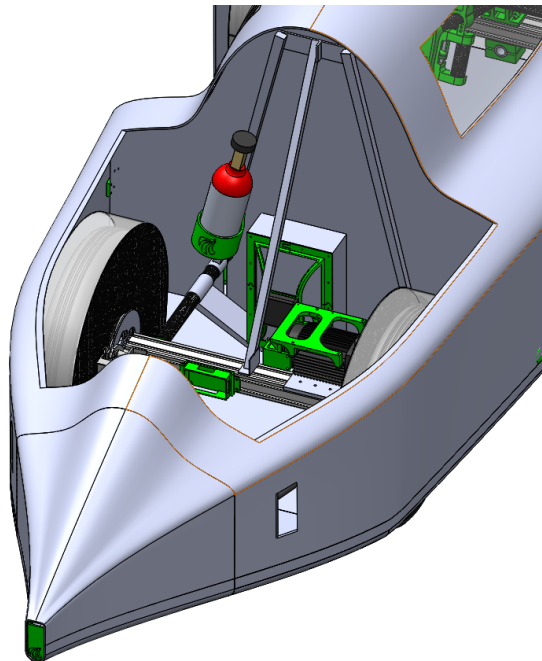


**Figure 6.1:** Figure showing the *trunk* of Cimbrer II, with the Mark1020 PEM fuel cell inside.

To evaluate the effect of increasing inlet temperature, a parametric study has been conducted. The tendency is the same for all operating currents, therefore, the study has been conducted using the average operating current doing the race in London in 2017. The stack current for one lap on the official track can be seen in figure 6.2.

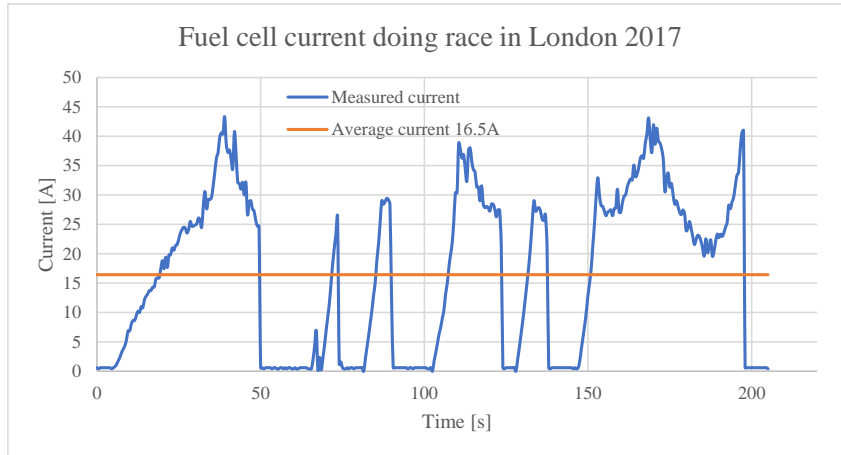


**Figure 6.2:** Figure showing the measured current doing one lap at the Shell Eco Marathon in London 2017.

The figure shows that the current peaks at approximately 45A. Doing one lap, the average current is approximately 16.5, the parametric study will, therefore, be conducted based on input parameters for that operating current. At first, a stoichiometry of 60 was used and the inlet temperature was varied from initially 25°C to 50°C with a 5°C temperature rise per simulation. The purpose of the flow rate through the stack is to supply sufficient amount of oxygen for the chemical reaction and to remove excess heat and maintaining an optimal operating temperature. The optimal operating temperature for the average current of 16.5A is approximately 46°C. A summarising table can be seen in 6.1.

**Table 6.1:** Table summarising the fixed input parameters.

Stack operating current	16.5 A
Cathode stoichiometry	60
Superficial inlet velocity	0.189 $m/s$
Outlet gauge pressure	0 Pa
Optimal operating temperature	46°C

As mentioned by [Andisheh-Tadbir et al., 2014], the optimal temperature of the stack is measured 88% down the length of the channel with respect to the inlet face. The temperature at this location has been determined from the numerical model and has been plotted with respect to the optimal stack temperature for that specific current as determined by [Ballard, 2009] and can be seen in figure 6.3 on the next page.

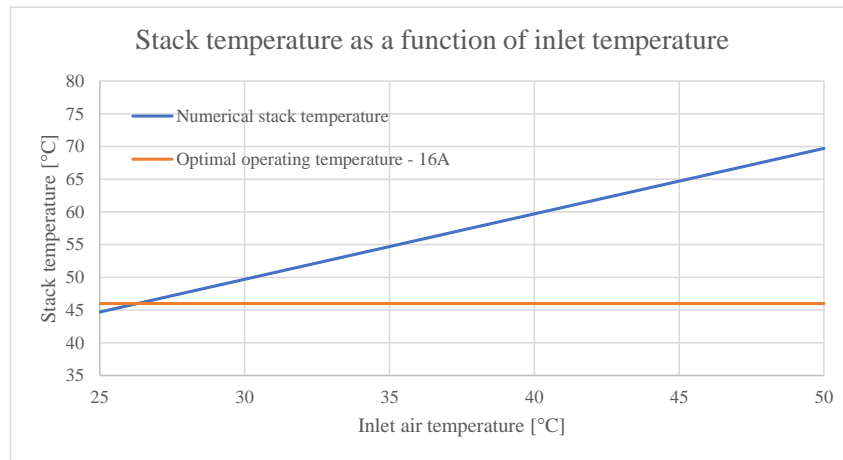


**Figure 6.3:** Figure showing the developing stack temperature as a function of inlet temperature.

It is evident from the figure, that the optimum stack temperature increases as a function of inlet temperature. A direct correlation between the inlet temperature and optimum stack temperature exist. That is that increase the inlet temperature by  $5^{\circ}\text{C}$  will increase the optimum stack temperature with  $5^{\circ}\text{C}$ . For the fuel cell to operate at an optimum temperature, for an average current of  $16.5\text{A}$  inlet temperature cannot increase further than approximately  $26.5^{\circ}\text{C}$ . Operating the stack at higher temperatures than the optimal temperature specified by [Ballard, 2009], increases the losses of the cell voltage. A figure showing the loss in cell voltage can be seen in figure 6.4. Where the losses for different currents can be seen as a function of how overheated the fuel cell stack is.

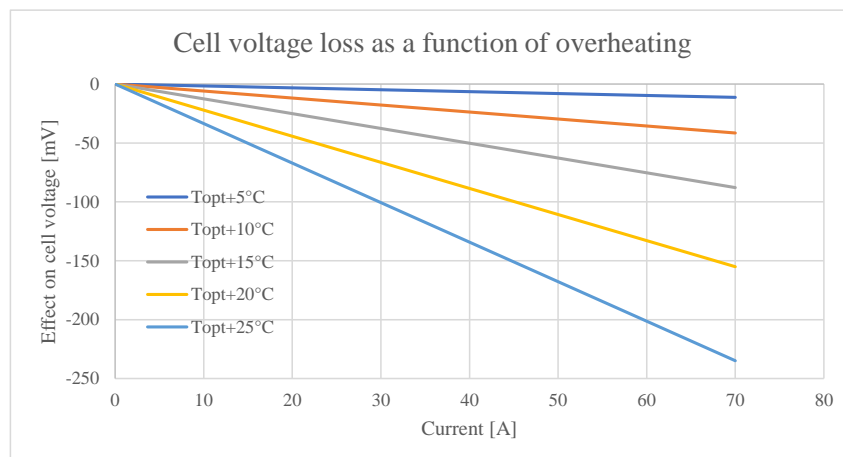


**Figure 6.4:** Figure showing the cell voltage loss, due to overheating, reproduced from [Ballard, 2009].

Figure 6.4 shows that an increasing stack temperature degrades the performance of the stack and is more severe at higher currents. The optimal temperature is already high, at high operating currents, therefore, a further increase in stack temperature damages the stack significantly [Ballard, 2009].

It is evident that maintaining an optimal operating temperature is of great importance for the fuel cell performance. Maintaining an optimal operating temperature, when the inlet temperature is increasing can be done by increasing the stoichiometry, hence, increasing the flow rate through the system leading to a higher heat transfer rate and thereby decreasing the stack temperature. To see the effect of changing the stoichiometry, a parametric study has been conducted. The inlet temperature has been set constant, while the stoichiometry is increased to see the effect of the optimal stack temperature. This has been done for a wide variety of inlet temperatures (25, 30, 35 and 40°C). The results can be seen in figure 6.5, where the optimal temperature for the average operating current doing the race 16.5A is plotted for comparison.

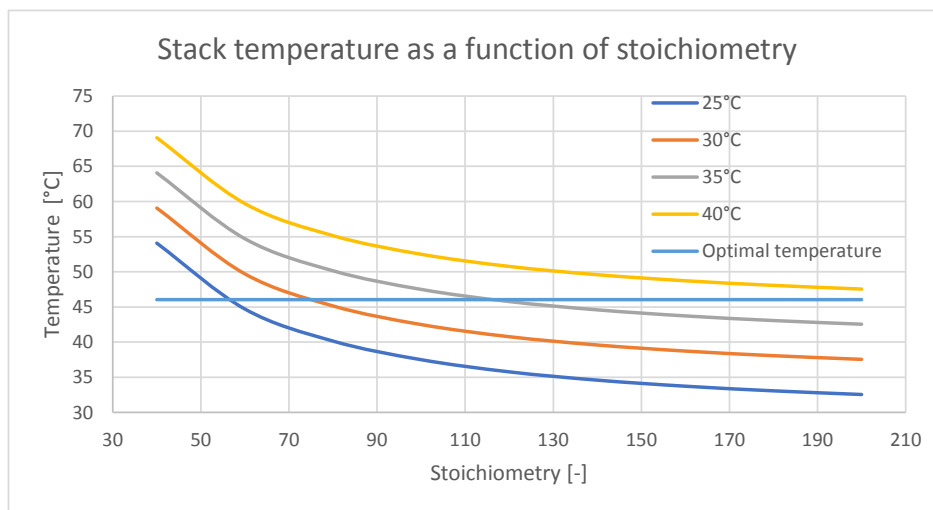


**Figure 6.5:** Figure showing the optimum stack temperature, as a function of stoichiometry.

The figure shows, that to maintain an optimal operating temperature for a current of 16.5A with increasing inlet temperature, the stoichiometry has to be increased. In the beginning, as the stoichiometry is increased for a fixed inlet temperature the optimum temperature decreases more rapidly than at higher stoichiometries at around 120.

This poses interesting possibilities, depending on the range of operating currents for the fuel cell system. It may be beneficial to increase the inlet temperature of the cathode side. Higher currents mean higher optimal temperature, and due to the more steep slope of the optimal temperature profile at lower stoichiometries increasing the temperature would impose fewer changes in volumetric flow rate to maintain an optimum temperature within a certain operating current range. Eventually, this leads to less energy being consumed by the fan and increases the systems overall efficiency.

## Discussion

# 7

The current fan used for pulling air through the Mark1020 fuel cell stack inside Cimbrer is an axial fan from Ebm-Papst. It is important to know the pressure and flow requirements over the entire range of currents, voltage, ambient temperature, etc. when sizing a fan.

The pressure drop over the porous media (cells) has been determined both empirically and numerically. It is, however, important to know the pressure drop for the entire system when choosing a fan. It is possible to determine the system pressure loss, that the fan has to overcome based on the numerical results. A table showing the pressure drop for the porous media (stack) and manifold part respectively can be seen in table 7.1. Simulations have been conducted for seven different operating currents. The corresponding volumetric flow rate is presented based on a stoichiometry of 60.

**Table 7.1:** Table displaying the pressure drop across the porous media and manifold.

<b>Current</b>	Flow rate	$\Delta P$ porous media	$\Delta P$ manifold	$\Delta P$ system
<i>A</i>	<i>m<sup>3</sup>/hr</i>	<i>Pa</i>	<i>Pa</i>	<i>Pa</i>
10	17.63	7.30	0.40	7.70
20	35.25	14.73	1.42	16.15
30	52.88	22.49	3.09	25.58
40	70.50	30.30	5.36	35.66
50	88.13	38.45	8.31	46.76
60	105.75	46.64	11.83	58.47
70	123.38	55.10	16.01	71.11

For fan sizing, a fan curve is utilised. The fan curve shows the relationship between the static pressure of the fan and the volumetric flow rate that it produces. The axial fan used for the current manifold configuration can be regulated using pulse width modulation (PWM). Meaning that it operates below the line of the fan curve.

To investigate in which area the fan is able to operate, the system pressure drop calculated in table 7.1 has been plotted together with the corresponding volumetric flow rate. These points have been visualised within the corresponding reproduced fan curve for Emb-Papst 8452/2 GHHP [Ebm-Papst, 2015] and can be seen in figure 7.1.

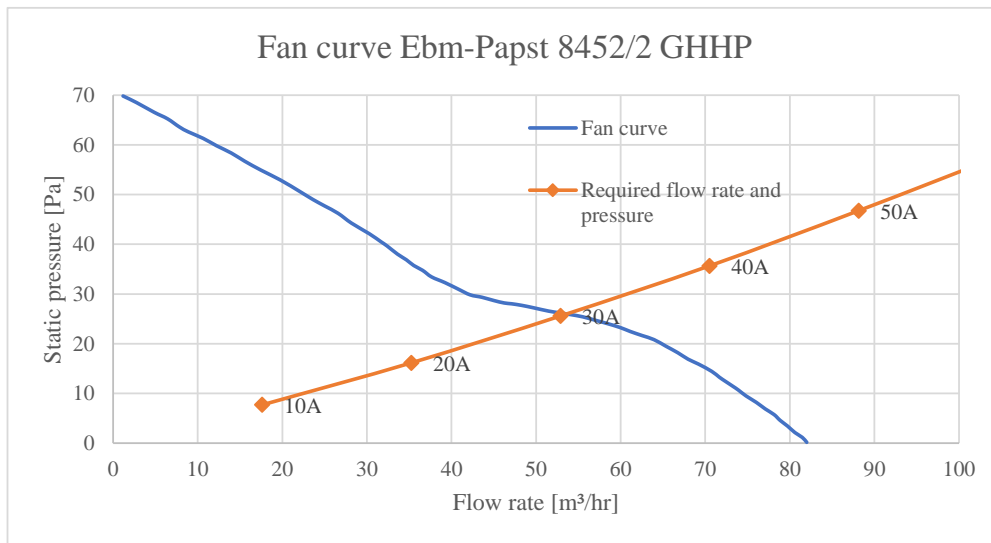


**Figure 7.1:** Figure showing the operating area for the current fan. Fan curve reproduced from [Ebm-Papst, 2015].

It is evident, from the figure that for currents higher than 30A the fan is not able to produce the required flow rate or overcome the system pressure drop. One way to overcome this with the current fan configuration is to lower the stoichiometry and hence decreasing the inlet flow rate and reducing the system pressure. However, according to [Ballard, 2011] stoichiometry below 20 results in degrading stack performance. A reproduced graph from [Ballard, 2009], shows the effect on cell voltage as a function of stoichiometry and can be seen in 7.2

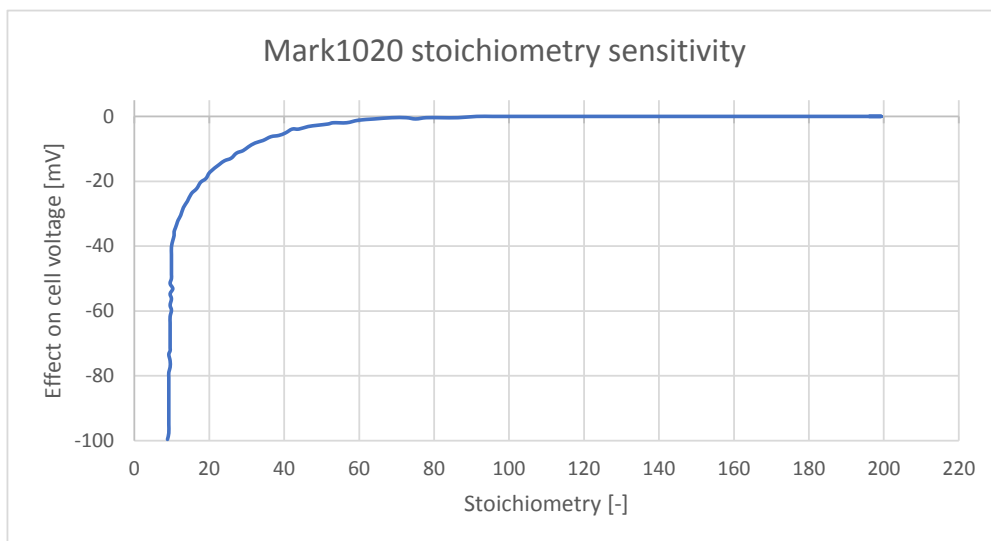


**Figure 7.2:** Figure showing the stoichiometry effect on the cell voltage. Graph reproduced from [Ballard, 2009].

Figure 7.2, shows that lowering the stoichiometry below 60 would increase the cell voltage losses. It can, therefore, be concluded that for currents higher than 30A the present fan would not be able to deliver the required volumetric flow rate or overcome the system pressure drop. However, lowering the stoichiometry would allow the fan to operate at currents higher than 30A but the cell voltage would drop decreasing the fuel cell performance and increasing the waste heat production.

## 7.1 Flow direction

Throughout this thesis, simulations of the fuel cell stack and manifold have been conducted with the fan placed downstream. According to [Ballard, 2011], a more uniform flow is achieved this way. It is possible to determine this from the numerical model, by letting the manifold outlet be the inlet of the system. Meaning that the fan is placed upstream instead of downstream. A figure showing the velocity magnitudes with the help of pathlines can be seen in 7.3.

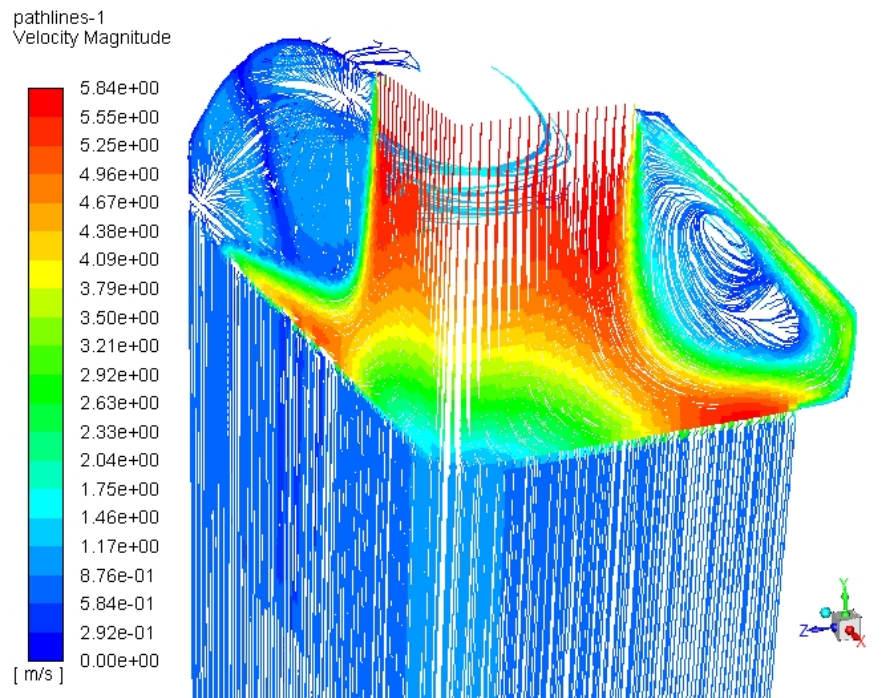


**Figure 7.3:** Pathlines showing the velocity magnitude in the manifold and porous media.

The figure shows large recirculation zones at the porous media inlet, this is due to the *pushing* of the air and significantly decreases the velocity through the stack. As a consequence, the optimal stack temperature is 2°C higher than for the same case with the fan placed downstream. The velocity distribution through the porous media significantly affects the temperature distribution in the XZ-plane. The temperature at the stack outlet differs with up to 4°C, compared to a very uniform temperature distribution with the fan placed downstream. A contour plot showing the outlet temperature of the stack can be seen in 7.4, where the highest temperature is at the edge of the stack.

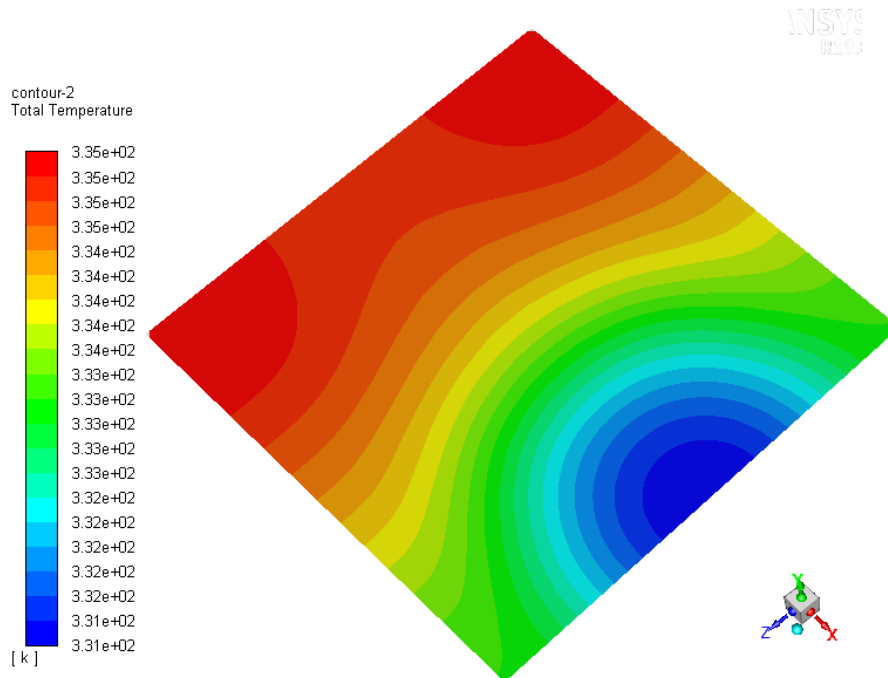


**Figure 7.4:** Contour plot of the stack exit temperature, the contour plot is the representation of half the actual stack.

There is substantial evidence, supporting the statement by [Ballard, 2011] saying that placing the fan downstream increases the uniformity in the flow.

## 7.2 Low flow velocity

During the numerical simulations, convergence troubles were observed when running simulations at low currents, hence, low flow rate. The residuals for continuity, velocity, and energy can be seen in figure 7.5 on the facing page.

Due to low velocities and low system pressure near the manifold outlet, reverse flow is observed. This reversed flow significantly affects the residuals, because the velocity magnitudes are small. This induces mass imbalance near the outlet surface of the system. However, observing the pressure drop and temperature across the porous media indicates a stable solution where the pressure and porous media temperature are converged.

It was observed that changing the outlet condition from a pressure outlet to a mass flow outlet, significantly stabilised the residuals by eliminating the reversed flow at the face outlet. However, convergence criteria of  $1 \cdot 10^{-3}$  were not reached but stabilised at around  $2 \cdot 10^{-3}$  for continuity.

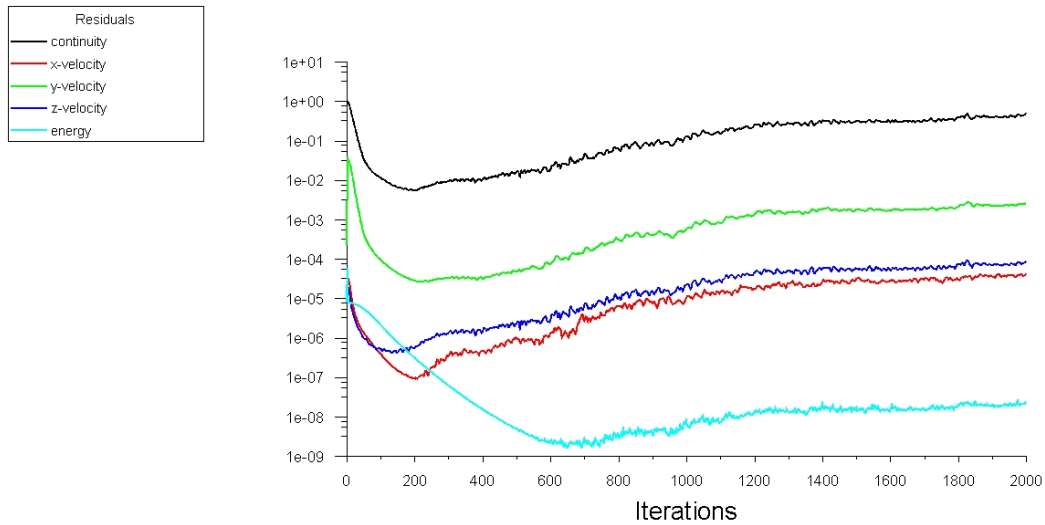


**Figure 7.5:** Residuals for simulation of 16.5A with a stoichiometry of 40. Convergence difficulties are observed.

### 7.3 Hub blockage

The numerical simulations were conducted with an open pressure outlet. In the real case, axial and tangential flow is present due to the rotation of the axial impeller. Also, the fan hub is present in the system acting as a blockage for the air trying to escape at the top of the manifold. Trying to capture the effect of the hub blockage, the geometry was redesigned as in figure 7.6

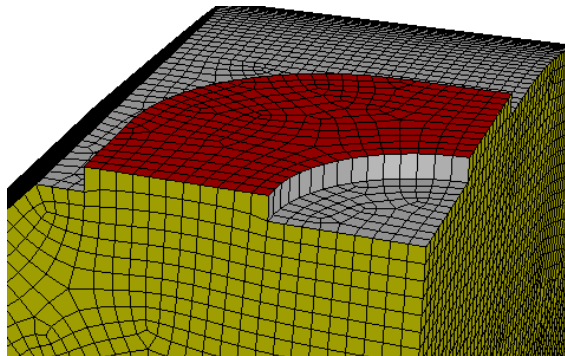


**Figure 7.6:** Figure showing the pressure outlet, with the hub blockage.

A base case of at 60A, with an inlet temperature of 25°C, was conducted and compared with the original case without the hub blockage. Simulations showed no changes over the porous zone, in terms of pressure or temperature. However, the total system pressure increased due to the addition of the fan blockage. The pressure drop across the manifold domain increased by 16% compared to the case without any hub blockage.

## 7.4 Manifold geometry

As shown in figure 5.5 on page 55, vorticity is observed at the corner of the manifold. The vorticity arises because the manifold is a little wider than the actual porous zone. To try and reduce or remove the vorticity, the corner is simply *cut off*. A base case has been conducted for 60A with an inlet temperature of 300K. The velocity contour for the symmetry plane of the porous zone has been displayed for both cases and can be seen in figure 7.7. Comparing these shows that cutting off the corner increases the velocity in at the very edge of the porous zone. This is entirely due to the fact that the flow no longer has to flow into the corner previously present due to the original manifold design.

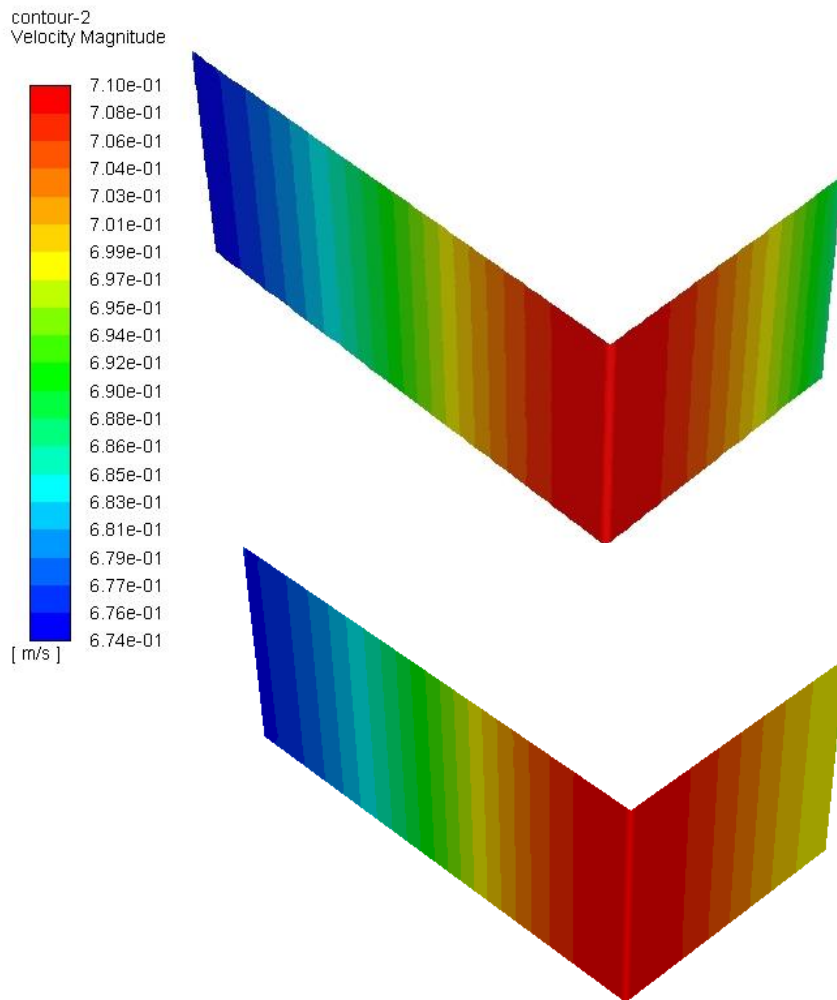


**Figure 7.7:** Contour plots showing the velocity magnitude through the porous zone, the contours displayed is  $1/4$  of the entire stack. Top one is the original manifold.

## Conclusions

# 8

The main objective of this master thesis is to investigate the flow distribution through the Mark1020 PEM fuel cell stack used for Team Aalborg Energy's hydrogen-powered car.

A numerical model has been constructed based on a porous media approach. The purpose of the porous media, was to reduce the computational time and number of cells. It can be concluded that the porous media model showed great coherence with the empirical results calculated from [Ballard, 2011]. The numerical model underpredicts the PEM fuel cell stack pressure drop by a maximum of 3.16% with an average difference of 2.87%. However, as mentioned at the beginning of chapter 6, a mistake has been made by not letting the density vary as a function of increasing temperature which would consequently increase the velocity through the stack and thereby increase the pressure drop.

It can be concluded from the numerical model, that the temperature distribution varies highly in the flow direction, but are almost constant in the plane, where an increasing current density would result in higher stack temperature, due to more heat being released. However, it can be concluded that the temperature distribution is too ideal compared to results from [Ballard, 2009] this may be due to the specified thermal conductivity of the solid.

It can be concluded from the numerical simulations, that blowing air through the stack is less efficient than pulling air through the stack by placing the fan downstream. Blowing air through the stack induced a high amount of vorticity at the cathode inlet reducing the flow rate through the stack and decreases the stack efficiency.

A parametric study were conducted to show the effect of temperature and stoichiometry. It can be concluded from the parametric study, that depending on the operating current range preheating of the inlet air may be beneficial due to the optimal operating temperature.

The total system pressure drop were determined from the numerical models and compared with the fan curve for the current fan used. It can be concluded, that for currents any higher than 30 amps the system starts to decrease in efficiency since the fan has to lower the stoichiometry. Small changes to the current manifold design showed to increase the flow velocity through the stack by around 2%.

It can be concluded, that using a porous media approach is a good way to estimate the flow distribution through a PEM fuel cell stack, instead of refining every single cell. The porous media approach can be used effectively to analyse the flow distribution and determine the pressure drop for a PEM fuel cell stack.



## Future work

---

The purpose of this chapter, is to outline the future work that may be conducted for this project. The numerical model constructed uses an ideal approach with regards to the pressure outlet. In the real case an axial fan is located at top of the manifold pulling air through the stack. Axial and tangential velocity will be present and may have significantly influence on the flow distribution through the fuel cell stack. Therefore, constructing a 3D fluid fan model could be an interesting way to investigate the influence of swirl for the flow distribution.

Another fascinating study would be to use anisotropic approach for the thermal conductivity to predict a more realistic temperature distribution through the stack. ANSYS Fluent allows the specification of the thermal conductivity by a 3x3 matrices, thereby allowing the user to effectively change the thermal conductivity in certain directions. This could be determined experimentally or through an trial an error by reproducing known temperature distributions.



## Bibliography

---

- Albring, 1967.** W. Albring. *An Introduction to Fluid Dynamics*. ZAMM - Journal of Applied Mathematics and Mechanics, 48(4), 1967. doi: 10.1002/zamm.19680480418.
- Andisheh-Tadbir et al., 2014.** Mehdi Andisheh-Tadbir, Andrew Desouza, Majid Bahrami and Erik Kjeang. *Cell level modeling of the hygrothermal characteristics of open cathode polymer electrolyte membrane fuel cells*. International Journal of Hydrogen Energy, 39(27), 14993 – 15004, 2014. ISSN 0360-3199. doi: <https://doi.org/10.1016/j.ijhydene.2014.07.049>. URL <http://www.sciencedirect.com/science/article/pii/S0360319914020084>.
- ANSYS, 2014.** ANSYS. *ANSYS convergence*, 2014. URL [http://www.grupossc.com/ponencias/ponencia\\_39114164442.pdf](http://www.grupossc.com/ponencias/ponencia_39114164442.pdf).
- ANSYS, 2018a.** ANSYS. *ANSYS Fluent Theory Guide*, 2018.
- ANSYS, 2018b.** ANSYS. *ANSYS Fluent User's Guide*, 2018.
- ANSYS, 2018c.** ANSYS. *ANSYS Meshing User's Guide*, 2018.
- Ballard, 2009.** Ballard. *Ballard1020 ACS - Product manual and integration guide*, 2009.
- Ballard, 2011.** Ballard. *Ballard1020 - Product manual and integration guide*, 2011.
- Barbir, 2005.** Frano Barbir. *PEM Fuel Cells: Theory and Practice*. Academic Press, 2005.
- Torsten Berning. Three-Dimensional Computational Analysis of Transport Phenomena in a PEM Fuel Cell. PhD thesis, University of Victoria, 1997.
- Berning, 2018.** Torsten Berning. *Mark1020 - Active Electrode Area*, 2018. Oral conversation about the active electrode area of the Mark1020 - PEM fuel cell stack.
- Choopanya and Yang, 2016.** P. Choopanya and Z. Yang. *An effective mesh strategy for CFD modelling of polymer electrolyte membrane fuel cells*. International Journal of Hydrogen Energy, 41(15), 6445 – 6456, 2016. ISSN 0360-3199. doi: <https://doi.org/10.1016/j.ijhydene.2016.03.016>. URL <http://www.sciencedirect.com/science/article/pii/S0360319915311186>.
- Ebm-Papst, 2015.** Ebm-Papst. *Product Data Sheet 8452/2 GHHP*, 2015. URL <https://docs-emea.rs-online.com/webdocs/12cd/0900766b812cdca1.pdf>.
- Xin Gao, Anders Christian Olesen and Søren Knudsen Kær. Thermal management optimization of an air-cooled hydrogen fuel cell system in an extreme environmental condition. In pres: By International Journal of Hydrogen Energy.
- Jeong et al., 10 2013.** Jeehoon Jeong, In-Su Han and Hyun Khil Shin. *Optimal Sizing of the Manifolds in a PEM Fuel Cell Stack using Three-Dimensional CFD Simulations*. International Journal of Hydrogen Energy, 24, 386–392, 2013.

- Jithin et al., 2017.** M. Jithin, Saurabh Siddharth, Malay K. Das and Ashoke De. *Simulation of coupled heat and mass transport with reaction in PEM fuel cell cathode using lattice Boltzmann method*. Thermal Science and Engineering Progress, 4, 85 – 96, 2017. ISSN 2451-9049. doi: <https://doi.org/10.1016/j.tsep.2017.09.004>. URL <http://www.sciencedirect.com/science/article/pii/S2451904916300348>.
- Macedo-Valencia et al., 2016.** J. Macedo-Valencia, J.M. Sierra, S.J. Figueroa-Ramírez, S.E. Díaz and M. Meza. *3D CFD modeling of a PEM fuel cell stack*. International Journal of Hydrogen Energy, 41(48), 23425 – 23433, 2016. ISSN 0360-3199. doi: <https://doi.org/10.1016/j.ijhydene.2016.10.065>. URL <http://www.sciencedirect.com/science/article/pii/S0360319916318687>.
- Mohan et al., 12 2004.** Ganesh Mohan, B Prabhakara Rao, Sarit Das, Pandiyan Subramaniam, N Rajalakshmi and K S Dhathathreyan. *Analysis of Flow Maldistribution of Fuel and Oxidant in a PEMFC*. Journal of Energy Resources Technology, 126, 2004.
- of Arizona.** *University of Arizona*. URL <http://cbc.chem.arizona.edu/~salzmanr/480a/480ants/gibshelm/gibshelm.html>.
- Ramani, 2006.** Vijay Ramani. *Fuel Cells*. The Electrochemical Society, 2006. URL [https://www.electrochem.org/dl/interface/spr/spr06/spr06\\_p41-44.pdf](https://www.electrochem.org/dl/interface/spr/spr06/spr06_p41-44.pdf).
- Schaschke, 2014.** Carl Schaschke. *A Dictionary of Chemical Engineering*. Oxford University, 2014.
- Shell, 2018.** *Shell*, 2018. URL <https://www.shell.com/energy-and-innovation/shell-ecomarathon/about.html>. Visited: 15-03-2018.
- Tu et al., 2007.** Jiyuan Tu, Guan-Heng Yeoh and Chaoqun Liu. *Computational fluid dynamics: a practical approach*. Butterworth-Heinemann, 2007.
- Versteeg and Malalasekera, 2007.** Henk Kaarle Versteeg and Weeratunge Malalasekera. *An introduction to computational fluid dynamics: the finite volume method*. Pearson Education, 2007.
- Wang et al., 2011.** Jinshi Wang, Junjie Yan, Jinliang Yuan and Bengt Sundén. *On Flow Maldistribution in PEMFC Stacks*. International Journal of Green Energy, 8(5), 585–606, 2011. doi: 10.1080/15435075.2011.576288. URL <https://doi.org/10.1080/15435075.2011.576288>.

## Appendix: Uploaded material

---



This appendix highlights the uploaded material.

Uploaded are two meshes, in the folder names (Meshes):

- Decomposed mesh, in the folder named.
- MultiZone mesh, used for simulations, in the folder names.

Uploaded case files, in the folder named (Case files) includes:

- Case for 10 A, with stoichiometry of 60.
- Case for 20 A, with stoichiometry of 60.
- Case for 30 A, with stoichiometry of 60.
- Case for 40 A, with stoichiometry of 60.
- Case for 50 A, with stoichiometry of 60.
- Case for 60 A, with stoichiometry of 60.
- Case for 70 A, with stoichiometry of 60.

Uploaded case files, in the folder named (Manifold with removed corner - Case file) includes:

- Manifold with the corner removed, for 60A and a stoichiometry of 60.

Uploaded case files, in the folder named (Blowing air) includes:

- Case file for blowing the air through the stack, at 60A and with a stoichiometry of 60.

Uploaded case files, in the folder named (With hub blockage) includes:

- Case file with hub blockage, for 60A and with a stoichiometry of 60.